

1

2

3

4

5

# Simultaneous Measurement of Oscillation Parameters in Beam and Atmospheric Neutrino Data from Tokai-to-Kamioka and Super-Kamiokande Experiments

6

Daniel Robert Clement Barrow

7

8

Magdalen College,  
Oxford University

9

Version 1.0

10

A Dissertation Submitted to Oxford University  
11 for the Degree of Doctor of Philosophy



13                   **Simultaneous Measurement of**  
14                   **Oscillation Parameters in Beam and**  
15                   **Atmospheric Neutrino Data from**  
16                   **Tokai-to-Kamioka and**  
17                   **Super-Kamiokande Experiments**

18                   *Abstract*

19                   Lorem ipsum dolor sit amet, consectetur adipiscing elit, sed do eiusmod tempor incididunt ut labore et dolore magna aliqua. Nulla aliquet porttitor lacus luctus accumsan tortor posuere. Pulvinar neque laoreet suspendisse interdum. Sem viverra aliquet eget sit. Nunc sed velit dignissim sodales ut eu sem integer vitae. At erat pellentesque adipiscing commodo elit at imperdiet dui accumsan. Fames ac turpis egestas integer eget aliquet nibh. Scelerisque eu ultrices vitae auctor eu augue. Purus non enim praesent elementum facilisis leo vel. Sollicitudin nibh sit amet commodo. Vitae auctor eu augue ut. Vel quam elementum pulvinar etiam. A condimentum vitae sapien pellentesque habitant morbi tristique senectus. Viverra accumsan in nisl nisi scelerisque eu ultrices. Sed viverra ipsum nunc aliquet bibendum enim. Sit amet purus gravida quis. In vitae turpis massa sed elementum tempus egestas sed sed. Vivamus arcu felis bibendum ut tristique et egestas. Senectus et netus et malesuada fames ac turpis. Ac auctor augue mauris augue.

35

## Declaration

36

This dissertation is the result of my own work, except where explicit reference is made to the work of others, and has not been submitted for another qualification to this or any other university. This dissertation does not exceed the word limit for the respective Degree Committee.

37

38

39

40

41

Daniel Robert Clement Barrow

42

43

44

45

46

©The copyright of this thesis rests with the author and is made available under a Creative Commons Attribution Non-Commercial No Derivatives licence. Researchers are free to copy, distribute or transmit the thesis on the condition that they attribute it, that they do not use it for commercial purposes and that they do not alter, transform or build upon it. For any reuse or redistribution, researchers must make clear to others the licence terms of this work.

47

## Acknowledgements

48 at pretium nibh ipsum. Eget nunc scelerisque viverra mauris in aliquam. Arcu vitae  
49 elementum curabitur vitae nunc sed velit dignissim. Sed arcu non odio euismod lacinia  
50 at quis risus sed. Vitae tempus quam pellentesque nec nam aliquam sem et tortor.  
51 Viverra aliquet eget sit amet tellus cras adipiscing. Purus sit amet luctus venenatis  
52 lectus magna. In aliquam sem fringilla ut morbi tincidunt augue. Fermentum dui  
53 faucibus in ornare. Aliquam malesuada bibendum arcu vitae elementum curabitur  
54 vitae nunc sed.

55 Ultricies leo integer malesuada nunc vel risus commodo. Tellus cras adipiscing  
56 enim eu turpis egestas pretium. Dictumst quisque sagittis purus sit amet volutpat  
57 consequat mauris nunc. Vitae congue mauris rhoncus aenean vel elit scelerisque  
58 mauris pellentesque. Vel facilisis volutpat est velit egestas dui id ornare. Suscipit  
59 adipiscing bibendum est ultricies. At in tellus integer feugiat scelerisque varius  
60 morbi enim. Cras semper auctor neque vitae tempus. Commodo sed egestas egestas  
61 fringilla phasellus faucibus. Cras pulvinar mattis nunc sed blandit. Pretium viverra  
62 suspendisse potenti nullam ac tortor vitae. Purus sit amet volutpat consequat. Orci  
63 sagittis eu volutpat odio facilisis mauris. Sit amet massa vitae tortor condimentum  
64 lacinia quis. Commodo sed egestas egestas fringilla phasellus. Sed libero enim sed  
65 faucibus turpis. Vitae tempus quam pellentesque nec.

66 Blandit massa enim nec dui. Viverra tellus in hac habitasse platea dictumst vestibulum.  
67 Bibendum enim facilisis gravida neque convallis. Sagittis nisl rhoncus mattis  
68 rhoncus urna neque. Nisl rhoncus mattis rhoncus urna neque. Ac tortor vitae purus  
69 faucibus ornare. Aenean sed adipiscing diam donec adipiscing tristique risus. Sapien  
70 nec sagittis aliquam malesuada bibendum. Et leo duis ut diam quam nulla. Tellus  
71 rutrum tellus pellentesque eu tincidunt tortor aliquam nulla facilisi. Fermentum leo  
72 vel orci porta non pulvinar neque. Eget sit amet tellus cras adipiscing enim eu. Sed  
73 viverra tellus in hac habitasse platea dictumst vestibulum.

74 Sit amet consectetur adipiscing elit. At varius vel pharetra vel turpis nunc eget  
75 lorem. Elit scelerisque mauris pellentesque pulvinar pellentesque habitant morbi  
76 tristique senectus. Odio euismod lacinia at quis risus sed vulputate odio. Vitae suscipit  
77 tellus mauris a diam maecenas sed enim ut. Dignissim convallis aenean et tortor at  
78 risus viverra. Diam sollicitudin tempor id eu. Erat velit scelerisque in dictum. Blandit  
79 cursus risus at ultrices. Ac tortor vitae purus faucibus ornare suspendisse sed.

# <sup>80</sup> Contents

<sup>81</sup> <b>1 Neutrino Oscillation Physics</b>	<sup>1</sup>
<sup>82</sup> 1.1 Discovery of Neutrinos . . . . .	<sup>1</sup>
<sup>83</sup> 1.2 Theory of Neutrino Oscillation . . . . .	<sup>2</sup>
<sup>84</sup> 1.2.1 Three Flavour Oscillations . . . . .	<sup>3</sup>
<sup>85</sup> 1.2.2 The MSW Effect . . . . .	<sup>6</sup>
<sup>86</sup> 1.3 Neutrino Oscillation Measurements . . . . .	<sup>7</sup>
<sup>87</sup> 1.3.1 Solar Neutrinos . . . . .	<sup>8</sup>
<sup>88</sup> 1.3.2 Atmospheric Neutrinos . . . . .	<sup>10</sup>
<sup>89</sup> 1.3.3 Accelerator Neutrinos . . . . .	<sup>12</sup>
<sup>90</sup> 1.3.4 Reactor Neutrinos . . . . .	<sup>15</sup>
<sup>91</sup> <b>2 T2K and SK Experiment Overview</b>	<sup>17</sup>
<sup>92</sup> 2.1 The Super-Kamiokande Experiment . . . . .	<sup>17</sup>
<sup>93</sup> 2.1.1 The SK Detector . . . . .	<sup>18</sup>
<sup>94</sup> 2.1.2 Calibration . . . . .	<sup>21</sup>
<sup>95</sup> 2.1.3 Data Acquisition and Triggering . . . . .	<sup>23</sup>
<sup>96</sup> 2.1.4 Cherenkov Radiation . . . . .	<sup>25</sup>
<sup>97</sup> 2.2 The Tokai to Kamioka Experiment . . . . .	<sup>26</sup>
<sup>98</sup> 2.2.1 The Neutrino Beam . . . . .	<sup>28</sup>
<sup>99</sup> 2.2.2 The Near Detector at 280m . . . . .	<sup>31</sup>
<sup>100</sup> 2.2.2.1 Fine Grained Detectors . . . . .	<sup>33</sup>
<sup>101</sup> 2.2.2.2 Time Projection Chambers . . . . .	<sup>34</sup>
<sup>102</sup> 2.2.2.3 $\pi^0$ Detector . . . . .	<sup>35</sup>
<sup>103</sup> 2.2.2.4 Electromagnetic Calorimeter . . . . .	<sup>36</sup>
<sup>104</sup> 2.2.2.5 Side Muon Range Detector . . . . .	<sup>38</sup>
<sup>105</sup> 2.2.3 The Interactive Neutrino GRID . . . . .	<sup>38</sup>
<sup>106</sup> <b>3 Bayesian Statistics Implemented Through Markov Chain Monte Carlo Techniques</b>	<sup>40</sup>
<sup>108</sup> 3.1 Bayesian Statistics . . . . .	<sup>41</sup>
<sup>109</sup> 3.2 Monte Carlo Simulation . . . . .	<sup>42</sup>
<sup>110</sup> 3.2.1 Markov Chain Monte Carlo . . . . .	<sup>43</sup>
<sup>111</sup> 3.2.2 Metropolis-Hastings Algorithm . . . . .	<sup>45</sup>

112	3.2.3 MCMC Optimisation . . . . .	46
113	3.3 Understanding the MCMC Results . . . . .	49
114	3.3.1 Marginalisation . . . . .	50
115	3.3.2 Parameter Estimation and Credible Intervals . . . . .	51
116	3.3.3 Application of Bayes' Theorem . . . . .	52
117	3.3.4 Comparison of MCMC Output to Expectation . . . . .	53
118	<b>4 Oscillation Probability Calculation</b>	55
119	4.1 Super-Kamiokande Methodology . . . . .	55
120	<b>Bibliography</b>	56
121	<b>List of Figures</b>	63
122	<b>List of Tables</b>	67



<sup>124</sup> **Chapter 1**

<sup>125</sup> **Neutrino Oscillation Physics**

<sup>126</sup> When first proposed, neutrinos were expected to be massless fermions that only in-  
<sup>127</sup> teract through weak and gravitational forces. This meant they were very difficult to  
<sup>128</sup> detect as they can pass through significant amounts of matter without interacting. De-  
<sup>129</sup> spite this, experimental neutrino physics has developed with many different detection  
<sup>130</sup> techniques and neutrino sources being used today. In direct tension with the standard  
<sup>131</sup> model physics, neutrinos have been determined to oscillate between different lepton  
<sup>132</sup> flavours requiring them to have mass.

<sup>133</sup> section 1.1 describes the observation techniques and discovery of neutrinos. The  
<sup>134</sup> theory underpinning neutrino oscillation is described in section 1.2. This section  
<sup>135</sup> includes the approximations which can be made to simplify the understanding of  
<sup>136</sup> neutrino oscillation in a two-flavour approximation as well as how the medium  
<sup>137</sup> in which neutrinos propagate can manipulate the oscillation probability. The past,  
<sup>138</sup> current, and future neutrino experiments are detailed in section 1.3 including the  
<sup>139</sup> reactor, atmospheric, and long-baseline accelerator neutrino sources that have been  
<sup>140</sup> used to successfully constrain oscillation parameter determination.

<sup>141</sup> **1.1 Discovery of Neutrinos**

<sup>142</sup> At the start of the 20<sup>th</sup> century, the electrons emitted from the  $\beta$ -decay of the nucleus  
<sup>143</sup> were found to have a continuous energy spectrum [1, 2]. This observation seemingly  
<sup>144</sup> broke the energy conservation invoked within that period's nuclear models. Postulated  
<sup>145</sup> in 1930 by Pauli as the solution to this problem, the neutrino (originally termed  
<sup>146</sup> "neutron") was theorized to be an electrically neutral spin-1/2 fermion with a mass of  
<sup>147</sup> the same order of magnitude as the electron [3]. This neutrino was to be emitted with  
<sup>148</sup> the electron in  $\beta$ -decay to alleviate the apparent breaking of energy conservation. As a  
<sup>149</sup> predecessor of the weak interaction model, Fermi's theory of  $\beta$ -decay developed the  
<sup>150</sup> understanding by coupling the four constituent particles; electron, proton, neutron,  
<sup>151</sup> and neutrino, into a consistent model [4].

Whilst Pauli was not convinced of the ability to detect neutrinos. The first observations of the particle were made in the mid-1950s when neutrinos from a reactor were observed via the inverse  $\beta$ -decay (IBD) process,  $\bar{\nu}_e + p \rightarrow n + e^+$  [5, 6]. The detector consisted of two parts; a neutrino interaction medium and a liquid scintillator. The interaction medium was built from two water tanks. These were loaded with cadmium chloride to allow increased efficiency of neutron capture. The positron emitted from IBD annihilates,  $e^+ + e^- \rightarrow 2\gamma$ , generating a prompt signal and the neutron is captured on the cadmium via  $n + {}^{108}Cd \rightarrow {}^{109}Cd \rightarrow {}^{109}Cd + \gamma$ , producing a delayed signal. The experiment observed an increase in the neutrino event rate when the reactor was operating compared to when it was switched off, in much the same way as modern reactor neutrino experiments operate.

After the discovery of the  $\nu_e$ , the natural question of how many flavours of neutrino exist was asked. In 1962, a measurement of the  $\nu_\mu$  was conducted at the Brookhaven National Laboratory [7]. A proton beam was directed at a beryllium target, generating a  $\pi$ -dominated beam which then decayed via  $\pi^\pm \rightarrow \mu^\pm + (\nu_\mu, \bar{\nu}_\mu)$ , and the subsequent interactions of the  $\nu_\mu$  were observed. The final observation to be made was that of the  $\nu_\tau$  from the DONUT experiment [8]. Three neutrinos seem the obvious solution as it mirrors the known number of charged lepton (as they form weak isospin doublets) but there could be evidence of more. Several neutrino experiments have found anomalous results [9, 10] which could be attributed to sterile neutrinos however cosmological observations indicate the number of neutrino species  $N_{eff} = 3.15 \pm 0.23$  [11].

## 1.2 Theory of Neutrino Oscillation

As direct evidence of beyond Standard Model physics, a neutrino generated with lepton flavour  $\alpha$  can change into a different lepton flavour  $\beta$  after propagating some distance. This phenomenon is called neutrino oscillation and requires that neutrinos must have a non-zero mass (as seen in subsection 1.2.1). This is direct evidence of beyond standard model physics. This behaviour has been characterised by the Pontecorvo-Maki-Nakagawa-Sakata (PMNS) [12–14] mixing matrix which describes how the flavour and mass of neutrinos are associated. This is analogous to the Cabibbo-Kobayashi-Maskawa (CKM) [15] matrix measured in quark physics.

---

### <sup>182</sup> 1.2.1 Three Flavour Oscillations

<sup>183</sup> The PMNS parameterisation defines three flavour eigenstates,  $\nu_e$ ,  $\nu_\mu$  and  $\nu_\tau$  (indexed  
<sup>184</sup>  $\nu_\alpha$ ), which are assigned based upon the weak interaction flavour states and three mass  
<sup>185</sup> eigenstates,  $\nu_1$ ,  $\nu_2$  and  $\nu_3$  (indexed  $\nu_i$ ). Each mass eigenstate is the superposition of all  
<sup>186</sup> three flavour states,

$$|\nu_i\rangle = \sum_{\alpha} U_{\alpha i} |\nu_{\alpha}\rangle. \quad (1.1)$$

<sup>187</sup>  $U$  is the PMNS matrix which correlates the mass and flavour eigenstates. Neutrinos  
<sup>188</sup> interact with leptons of the same weak flavour eigenstate rather than mass eigenstate.  
<sup>189</sup> The propagation of a neutrino flavour eigenstate, in a vacuum, can be re-written as a  
<sup>190</sup> plane-wave solution to the time-dependent Schrödinger equation,

$$|\nu_{\alpha}(t)\rangle = \sum_i U_{\alpha i}^* |\nu_i\rangle e^{-i\phi_i}. \quad (1.2)$$

<sup>191</sup> The probability of observing a neutrino of flavour eigenstate  $\beta$  from one which  
<sup>192</sup> originated as flavour  $\alpha$  can be calculated as,

$$P(\nu_{\alpha} \rightarrow \nu_{\beta}) = |\langle \nu_{\beta} | \nu_{\alpha}(t) \rangle|^2 = \sum_{i,j} U_{\alpha i}^* U_{\beta i} U_{\alpha j} U_{\beta j}^* e^{-i(\phi_j - \phi_i)} \quad (1.3)$$

<sup>193</sup> The  $\phi_i$  term can be expressed in terms of the energy,  $E_i$ , and magnitude of the  
<sup>194</sup> three momenta,  $p_i$ , of the neutrino,  $\phi_i = E_i t - p_i x$  ( $t$  and  $x$  being time and position  
<sup>195</sup> coordinates). Therefore,

$$\phi_j - \phi_i = E_j t - E_i t - p_j x + p_i x. \quad (1.4)$$

<sup>196</sup> For a relativistic particle,  $E_i \gg m_i$ ,

$$p_i = \sqrt{E_i^2 - m_i^2} \approx E_i - \frac{m_i^2}{2E_i}. \quad (1.5)$$

<sup>197</sup> Making the approximations that neutrinos are relativistic, the mass eigenstates  
<sup>198</sup> were created with the same energy and that  $x = L$ , where  $L$  is the distance traveled by  
<sup>199</sup> the neutrino, Equation 1.4 then becomes

$$\phi_j - \phi_i = \frac{\Delta m_{ij}^2 L}{2E}, \quad (1.6)$$

<sup>200</sup> where  $\Delta m_{ij}^2 = m_i^2 - m_j^2$ . This, teamed with further use of unitarity relations results  
<sup>201</sup> in Equation 1.3 becoming

$$P(\nu_\alpha \rightarrow \nu_\beta) = \delta_{\alpha\beta} - 4 \sum_{i>j} \Re \left( U_{\alpha i}^* U_{\beta i} U_{\alpha j} U_{\beta j}^* \right) \sin^2 \left( \frac{\Delta m_{ij}^2 L}{4E} \right) + (-) 2 \sum_{i>j} \Im \left( U_{\alpha i}^* U_{\beta i} U_{\alpha j} U_{\beta j}^* \right) \sin \left( \frac{\Delta m_{ij}^2 L}{2E} \right). \quad (1.7)$$

<sup>202</sup> Where  $\delta_{\alpha\beta}$  is the Kronecker delta function and the negative sign is included for the  
<sup>203</sup> oscillation probability of antineutrinos.

<sup>204</sup> Typically, the PMNS matrix is parameterised into three mixing angles, a charge  
<sup>205</sup> parity (CP) violating phase  $\delta_{CP}$ , and two Majorana phases  $\alpha_{1,2}$ ,

$$U = \underbrace{\begin{pmatrix} 1 & 0 & 0 \\ 0 & c_{23} & s_{23} \\ 0 & -s_{23} & c_{23} \end{pmatrix}}_{\text{Atmospheric, Accelerator}} \underbrace{\begin{pmatrix} c_{13} & 0 & s_{13}e^{-i\delta_{CP}} \\ 0 & 1 & 0 \\ -s_{13}e^{-i\delta_{CP}} & 0 & c_{13} \end{pmatrix}}_{\text{Reactor, Accelerator}} \underbrace{\begin{pmatrix} c_{12} & s_{12} & 0 \\ -s_{12} & c_{12} & 0 \\ 0 & 0 & 1 \end{pmatrix}}_{\text{Reactor, Solar}} \underbrace{\begin{pmatrix} e^{i\alpha_1/2} & 0 & 0 \\ 0 & e^{i\alpha_2/2} & 0 \\ 0 & 0 & 1 \end{pmatrix}}_{\text{Majorana}}. \quad (1.8)$$

206 Where  $s_{ij} = \sin(\theta_{ij})$  and  $c_{ij} = \cos(\theta_{ij})$ . The oscillation parameters are often  
 207 grouped; (1,2) as “solar”, (2,3) as “atmospheric” and (1,3) as “reactor”. Many  
 208 neutrino experiments aim to measure the PMNS parameters from a wide array of  
 209 origins, as is the purpose of this thesis.

210 The Majorana phase,  $\alpha_{1,2}$ , containing matrix included within Equation 1.8 is only  
 211 included for completeness. For an oscillation analysis experiment, any term in this  
 212 oscillation probability calculation containing this phase disappears due to taking the  
 213 expectation value of the PMNS matrix.

214 A two flavour approximation can be attained when one assumes the third mass  
 215 eigenstate is degenerate with another. As discussed in section 1.3, it is found that  
 216  $\Delta m_{21}^2 \ll |\Delta m_{31}^2|$ . This results in the two flavour approximation being reasonable for  
 217 understanding the features of the oscillation. In this two flavour case, the mixing  
 218 matrix becomes,

$$U_{2\text{ Flav.}} = \begin{pmatrix} \cos(\theta) & \sin(\theta) \\ -\sin(\theta) & \cos(\theta) \end{pmatrix}. \quad (1.9)$$

219 This culminates in the oscillation probability,

$$\begin{aligned} P(\nu_\alpha \rightarrow \nu_\alpha) &= 1 - \sin^2(2\theta) \sin^2\left(\frac{\Delta m^2 L}{4E}\right), \\ P(\nu_\alpha \rightarrow \nu_\beta) &= \sin^2(2\theta) \sin^2\left(\frac{\Delta m^2 L}{4E}\right). \end{aligned} \quad (1.10)$$

220 For  $\alpha \neq \beta$ . For a fixed neutrino energy, the oscillation probability is a sinusoidal  
 221 function depending upon the distance over which the neutrino propagates. The  
 222 frequency and amplitude of oscillation are dependent upon the ratio of the  $\Delta m^2/4E$   
 223 and  $\sin^2 2\theta$ , respectively. For more human-readable units, the maximum oscillation  
 224 probability for a fixed value of  $\theta$  is given at  $L[\text{km}]/E[\text{GeV}] \sim 1.27/\Delta m^2$ . It is this  
 225 calculation that determines the best  $L/E$  value for a given experiment to be designed  
 226 around for measurements of a specific value of  $\Delta m^2$ .

---

### <sup>227</sup> 1.2.2 The MSW Effect

<sup>228</sup> The theory of neutrino oscillation in a vacuum is described in subsection 1.2.1. How-  
<sup>229</sup> ever, the beam neutrinos and atmospheric neutrinos originating from below the  
<sup>230</sup> horizon propagate through matter in the Earth. The coherent scattering of neutrinos  
<sup>231</sup> from a material target modifies the hamiltonian of the system. This results in a change  
<sup>232</sup> in the oscillation probability. Notably, charged current scattering ( $\nu_e + e^- \rightarrow \nu_e + e^-$ ,  
<sup>233</sup> propagated by a  $W$  boson) only affects electron neutrinos compared to the neutral  
<sup>234</sup> current scattering ( $\nu_l + l^- \rightarrow \nu_l + l^-$ , propagated by a  $Z^0$  boson), interacts through  
<sup>235</sup> all neutrino flavours equally. In the two-flavour limit, the effective mixing parameter  
<sup>236</sup> becomes

$$\sin^2(2\theta) \rightarrow \sin^2(2\theta_m) = \frac{\sin^2(2\theta)}{(A/\Delta m^2 - \cos(2\theta))^2 + \sin^2(2\theta)}, \quad (1.11)$$

<sup>237</sup> where  $A = 2\sqrt{2}G_F N_e E$  with  $N_e$  is the electron density of the medium and  $G_F$  is  
<sup>238</sup> Fermi's constant. It is clear to see that there exists a value of  $A = \Delta m^2 \cos(2\theta)$  for  
<sup>239</sup>  $\Delta m^2 > 0$  which results in a divergent mixing parameter. This resonance is due to  
<sup>240</sup> the Mikheyev-Smirnov-Wolfenstein (MSW) effect (or more colloquially, the matter  
<sup>241</sup> resonance) which regenerates the electron neutrino component of the neutrino flux  
<sup>242</sup> [16–18]. The density at which the resonance occurs is given by

$$N_e = \frac{\Delta m^2 \cos(2\theta)}{2\sqrt{2}G_F E}. \quad (1.12)$$

<sup>243</sup> At densities lower than this critical value, the oscillation probability will be much  
<sup>244</sup> closer to that of vacuum oscillation. The resonance occurring from the MSW effect  
<sup>245</sup> depends on the sign of  $\Delta m^2$ . Therefore, any neutrino oscillation experiment which  
<sup>246</sup> observes neutrinos and antineutrinos which have propagated through matter can have  
<sup>247</sup> some sensitivity to the ordering of the neutrino mass eigenstates.

<sup>248</sup> For an experiment observing atmospheric neutrinos propagating through the Earth,  
<sup>249</sup> such as the studies presented in this thesis, a model of the Earth's density and layering  
<sup>250</sup> is required. The model used within this analysis is the Preliminary Reference Earth

251 Model (PREM) [19]. This model provides piecewise cubic polynomials. To follow the  
252 methodology set in [20], this analysis simply approximates the model as four layers of  
253 constant density with values taken from the PREM model, as described in Table 1.1.  
254 As seen in DB: [Link to Oscillation chapter](#), the approximation in this methodology has  
255 been removed and the density is instead integrated along the track using the piecewise  
256 polynomials.

257 The density measurements provided in the PREM model are provided in terms  
258 of mass density, whereas neutrino oscillations are sensitive to the electron number  
259 density. This value can be computed as the product of the chemical composition and  
260 mass density of each layer.

Layer	Outer Radius [km]	Density [g/cm <sup>3</sup> ]	Chemical composition (Z/A)
Inner Core	1220	13	$0.468 \pm 0.029$
Outer Core	3480	11.3	$0.468 \pm 0.029$
Lower Mantle	5701	5.0	0.497
Transition Zone	6371	3.3	0.497

**Table 1.1:** Description of the four layers of the Earth invoked within the PREM model [19].

261 The beam oscillation probability in this thesis uses a baseline of 295km, density  
262 2.6g/cm<sup>3</sup>, and chemical composition 0.5.

### 263 1.3 Neutrino Oscillation Measurements

264 As evidence of beyond standard model physics, the 2015 Nobel Prize in Physics was  
265 awarded to the Super-Kamiokande (SK) [21] and Sudbury Neutrino Observatory  
266 (SNO) [22] collaborations for the first definitive observation of solar and atmospheric  
267 neutrino oscillation [23]. Since then, the field has seen a wide array of oscillation  
268 measurements from a variety of neutrino sources. As seen in subsection 1.2.1, the  
269 neutrino oscillation probability is dependent on the ratio of the propagation baseline,  $L$ ,  
270 to the neutrino energy,  $E$ . It is this ratio that determines the type of neutrino oscillation  
271 a particular experiment is sensitive to.

272 As illustrated in Figure 1.1, there are many neutrino sources that span a wide  
273 range of energies. The least energetic neutrinos are from diffuse supernovae and

<sup>274</sup> terrestrial neutrinos at  $O(1)$ MeV whereas the most energetic neutrinos originate from  
<sup>275</sup> atmospheric and galactic neutrinos of  $> O(1)$ TeV.

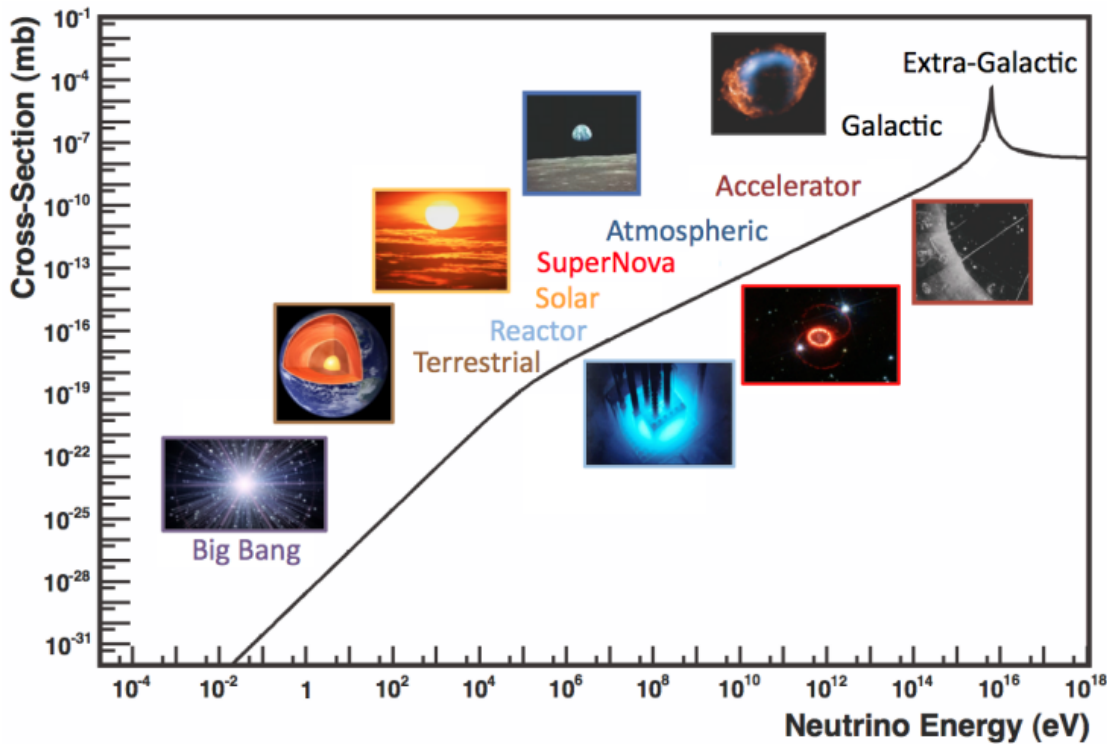


**Figure 1.1:** The cross-section of neutrinos from various natural and man-made sources as a function of neutrino energy. Taken from [24]

### <sup>276</sup> 1.3.1 Solar Neutrinos

<sup>277</sup> Solar neutrinos are emitted from fusion reaction chains at the center of the Sun. The  
<sup>278</sup> solar neutrino flux, given as a function of neutrino energy for different fusion and  
<sup>279</sup> decay chains is illustrated in Figure 1.2. Whilst proton-proton fusion generates the  
<sup>280</sup> largest flux of neutrinos, the neutrinos are of low energy and are difficult to reconstruct  
<sup>281</sup> due to the IBD interaction threshold of 1.8MeV. Consequently, most experiments focus  
<sup>282</sup> on the neutrinos from the decay of  ${}^8B$  (via  ${}^8B \rightarrow {}^8Be^* + e^+ + \nu_e$ ), which are higher  
<sup>283</sup> energy.

<sup>284</sup> The first measurements of solar neutrinos observed a significant reduction in the  
<sup>285</sup> event rate compared to predictions from the Standard Solar Model [26, 27]. The  
<sup>286</sup> proposed solution to this “solar neutrino problem” was  $\nu_e \leftrightarrow \nu_\mu$  oscillations in a

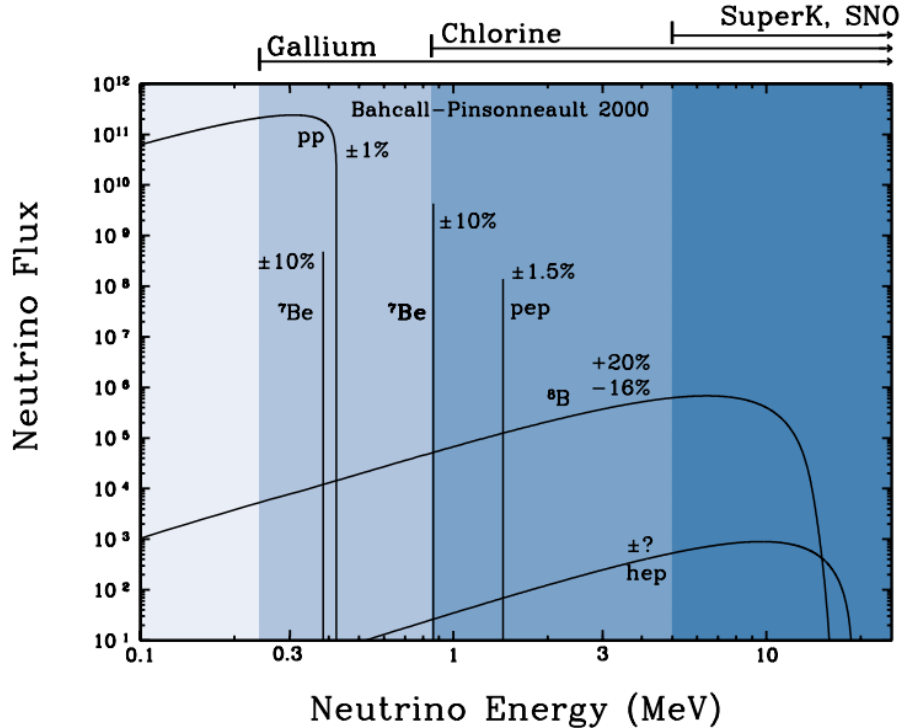


**Figure 1.2:** The solar neutrino flux as a function of neutrino energy for various fusion reactions and decay chains as predicted by the Standard Solar Model. Taken from [25].

<sup>287</sup> precursory version of the PMNS model [28]. The Kamiokande [29], Gallex [30] and  
<sup>288</sup> Sage [31] experiments confirmed the  $\sim 0.5$  factor deficit of solar neutrinos.

<sup>289</sup> The conclusive solution to this problem was determined by the SNO collaboration  
<sup>290</sup> [32]. Using a deuterium water target to observe  ${}^8B$  neutrinos, the event rate of  
<sup>291</sup> charged current (CC), neutral current (NC), and elastic scattering (ES) interactions  
<sup>292</sup> (Given in Equation 1.13) was simultaneously measured. CC events can only occur for  
<sup>293</sup> electron neutrinos, whereas the other interaction channels are agnostic to neutrino  
<sup>294</sup> flavour (Although the ES reaction is more sensitive to electron neutrino interactions).  
<sup>295</sup> This meant that there were direct measurements of the  $\nu_e$  and  $\nu_x$  neutrino flux. It  
<sup>296</sup> was concluded that the CC and ES interaction rates were consistent with the deficit  
<sup>297</sup> previously observed. Most importantly, the NC reaction rate was only consistent with  
<sup>298</sup> the others under the hypothesis of flavour transformation.

$$\begin{aligned}
 \nu_e + d &\rightarrow p + p + e^- & (CC) \\
 \nu_x + d &\rightarrow p + n + \nu_x & (NC) \\
 \nu_x + e^- &\rightarrow \nu_x + e^- & (ES)
 \end{aligned} \tag{1.13}$$

Many experiments have since measured the neutrino flux of different interaction chains within the sun [33–35]. The most recent measurement was that of CNO neutrinos which were recently observed with  $5\sigma$  significance by the Borexino collaboration. Future neutrino experiments aim to further these spectroscopic measurements of different fusion chains within the Sun [36–38]. Solar neutrinos act as an irreducible background for dark matter experiments like DARWIN but oscillation parameter measurements can be made [39].

### 1.3.2 Atmospheric Neutrinos

The interactions of primary cosmic ray protons in Earth's upper atmosphere generate showers of energetic hadrons. These are mostly pions and kaons which when they decay produce a natural source of neutrinos spanning energies of MeV to TeV [40]. This decay is via

$$\begin{aligned}
 \pi^\pm &\rightarrow \mu^\pm + (\nu_\mu, \bar{\nu}_\mu) \\
 \mu^\pm &\rightarrow e^\pm + (\nu_\mu, \bar{\nu}_\mu) + (\nu_e, \bar{\nu}_e)
 \end{aligned} \tag{1.14}$$

such that for a single pion decay, three neutrinos are produced. The atmospheric neutrino flux energy spectra as predicted by the Bartol [41], Honda [42, 43], and FLUKA [44] models are illustrated in Figure 1.3. The flux distribution peaks at an energy of  $O(10)$ GeV. The uncertainties associated with these models are dominated by the hadronic production of kaon and pions as well as the primary cosmic flux.

Unlike long-baseline experiments which have a fixed baseline, the distance atmospheric neutrinos propagate is dependent upon the zenith angle at which they interact. This is illustrated in Figure 1.4. Neutrinos that are generated directly above the detector ( $\cos(\theta) = 1.0$ ) have a baseline equivalent to the height of the atmosphere whereas neutrinos that interact directly below the detector ( $\cos(\theta) = -1.0$ ) have to

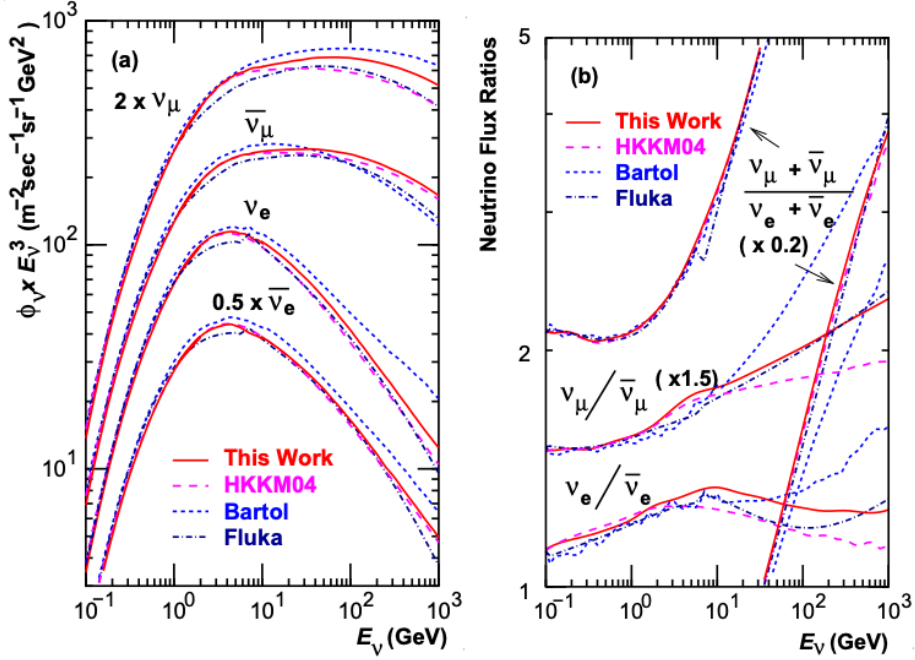


**Figure 1.3:** Left panel: The atmospheric neutrino flux for different neutrino flavours as a function of neutrino energy as predicted by the 2007 Honda model (“This work”) [42], the 2004 Honda model (“HKKM04”) [43], the Bartol model [41] and the FLUKA model [44]. Right panel: The ratio of the muon to electron neutrino flux as predicted by all the quoted models. Both figures taken from [42].

321 travel a length equal to the diameter of the Earth. This means atmospheric neutrinos  
 322 have a baseline that varies from  $O(20)$ km to  $O(6 \times 10^3)$ km. Any neutrino generated  
 323 at or below the horizon will be subject to matter effects as they propagate through the  
 324 Earth.

325 Figure 1.5 highlights the neutrino flux as a function of the zenith angle for different  
 326 slices of neutrino energy. For medium to high-energy neutrinos (and to a lesser degree  
 327 for low-energy neutrinos), the flux is approximately symmetric around  $\cos(\theta) = 0$ .  
 328 To the accuracy of this approximation, the systematic uncertainties associated with  
 329 atmospheric flux for comparing upward-going and down-going neutrino cancels. This  
 330 allows the down-going events, which are mostly insensitive to oscillation probabilities,  
 331 to act as an unoscillated prediction (similar to a near detector in an accelerator neutrino  
 332 experiment).

333 Precursory hints of atmospheric neutrinos were observed in the mid-1960s search-  
 334 ing for  $\nu_\mu^{(-)} + X \rightarrow X^* + \mu^\pm$  [46]. This was succeeded with the IMB-3 [47] and  
 335 Kamiokande [48] experiments which measured the ratio of muon neutrinos com-  
 336 pared to electron neutrinos  $R(\nu_\mu / \nu_e)$ . Both experiments were found to have a con-

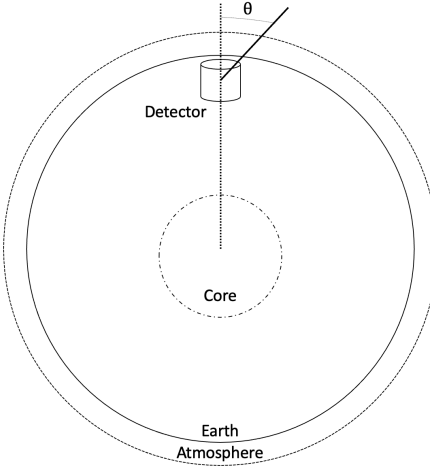


**Figure 1.4:** A diagram illustrating the definition of zenith angle as used in the Super Kamiokande experiment [45].

<sup>337</sup> sistent deficit of muon neutrinos, with  $R(\nu_\mu/\nu_e) = 0.67 \pm 0.17$  and  $R(\bar{\nu}_\mu/\bar{\nu}_e) =$   
<sup>338</sup>  $0.60^{+0.07}_{-0.06} \pm 0.05$ . Super-Kamiokande (SK) [45] extended this analysis by fitting os-  
<sup>339</sup> cillation parameters in  $P(\nu_\mu \rightarrow \nu_\tau)$  which found best fit parameters  $\sin^2(2\theta) > 0.92$   
<sup>340</sup> and  $1.5 \times 10^{-3} < \Delta m^2 < 3.4 \times 10^{-3} \text{ eV}^2$ .

<sup>341</sup> Since then, atmospheric neutrino experiments have been making precision mea-  
<sup>342</sup> surements of the  $\sin^2(\theta_{23})$  and  $\Delta m^2_{32}$  oscillation parameters. Atmospheric neutrino  
<sup>343</sup> oscillation is dominated by  $P(\nu_\mu \rightarrow \nu_\tau)$ , where SK observed a  $4.6\sigma$  discovery of  $\nu_\tau$   
<sup>344</sup> appearance [49]. Figure 1.6 illustrates the current estimates on the atmospheric mixing  
<sup>345</sup> parameters from a wide range of atmospheric and accelerator neutrino observatories.

### <sup>346</sup> 1.3.3 Accelerator Neutrinos

<sup>347</sup> The concept of using a man-made “neutrino beam” was first realised in 1962 [56].  
<sup>348</sup> Since then, many experiments have followed which all use the same fundamental  
<sup>349</sup> concepts. Typically, a proton beam is aimed at a target producing charged mesons that  
<sup>350</sup> decay to neutrinos. The mesons can be sign-selected by the use of magnetic focusing  
<sup>351</sup> horns to generate a neutrino or antineutrino beam. Pions are the primary meson that  
<sup>352</sup> decay and depending on the orientation of the magnetic field, a muon (anti-)neutrino  
<sup>353</sup> beam is generated via  $\pi^+ \rightarrow \mu^+ + \nu_\mu$  or  $\pi^- \rightarrow \mu^- + \bar{\nu}_\mu$ . The decay of muons and  
<sup>354</sup> kaons does result in an irreducible intrinsic electron neutrino background. In T2K,  
<sup>355</sup> this background contamination is  $O(< 1\%)$  [57]. There is also an approximately  $\sim 5\%$   
<sup>356</sup> “wrong-sign” neutrino background of  $\bar{\nu}_\mu$  generated via the same decays.

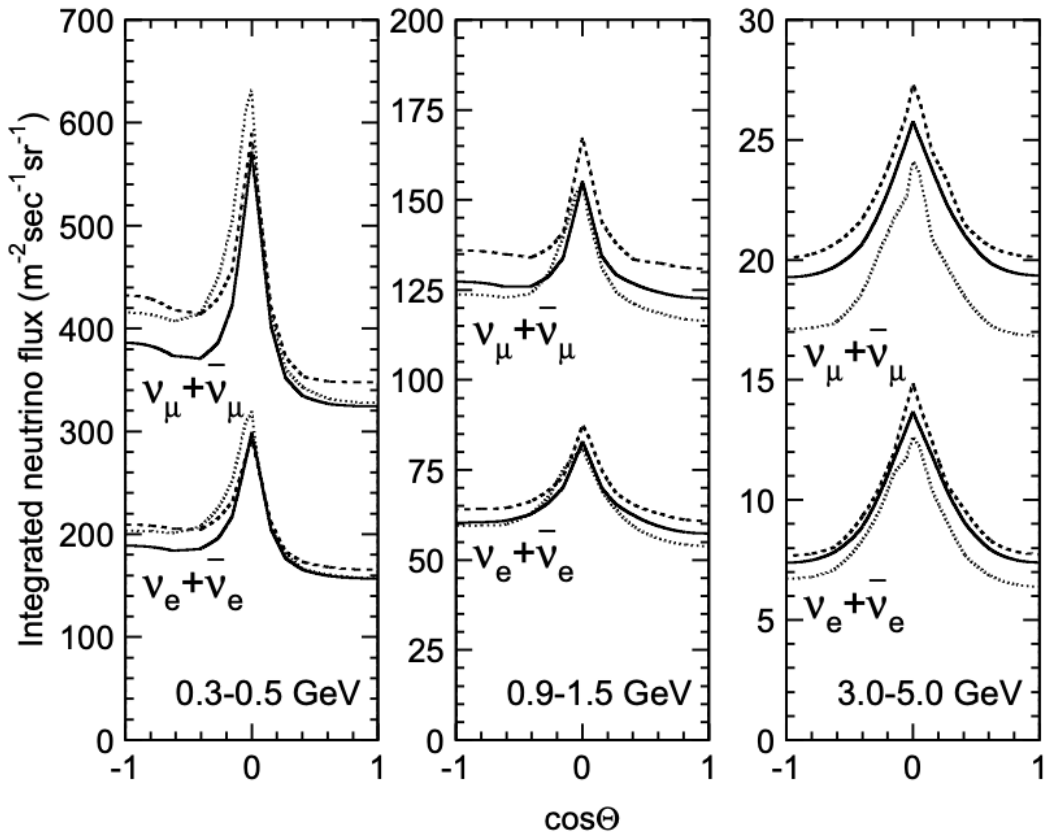


**Figure 1.5:** Predictions of the summed neutrino and antineutrino flux for electron and muon neutrinos from the Bartol [41], Honda [42] and FLUKA [44] models as a function of zenith angle with respect to the detector. Left panel:  $0.3 < E_\nu < 0.5$ . Middle panel:  $0.9 < E_\nu < 1.5$ . Right panel:  $3.0 < E_\nu < 5.0$ . Figures taken from [45].

The energy of each neutrino in the beam is dependent on the energy of the initial proton beam. Therefore, tuning the proton energy allows the neutrino energy to be set to a value that maximises the disappearance oscillation probability in the  $L/E$  term in Equation 1.10. This means that accelerator experiments are typically more sensitive to the mixing parameters as compared to a natural neutrino source. However, the disadvantage compared to atmospheric neutrino experiments is that the baseline has to be shorter due to the lower flux. Consequently, there is typically less sensitivity to matter effects and the ordering of the neutrino mass eigenstates.

A neutrino experiment measures

$$R(\vec{x}) = \Phi(E_\nu) \times \sigma(E_\nu) \times \epsilon(\vec{x}) \times P(\nu_\alpha \rightarrow \nu_\beta), \quad (1.15)$$

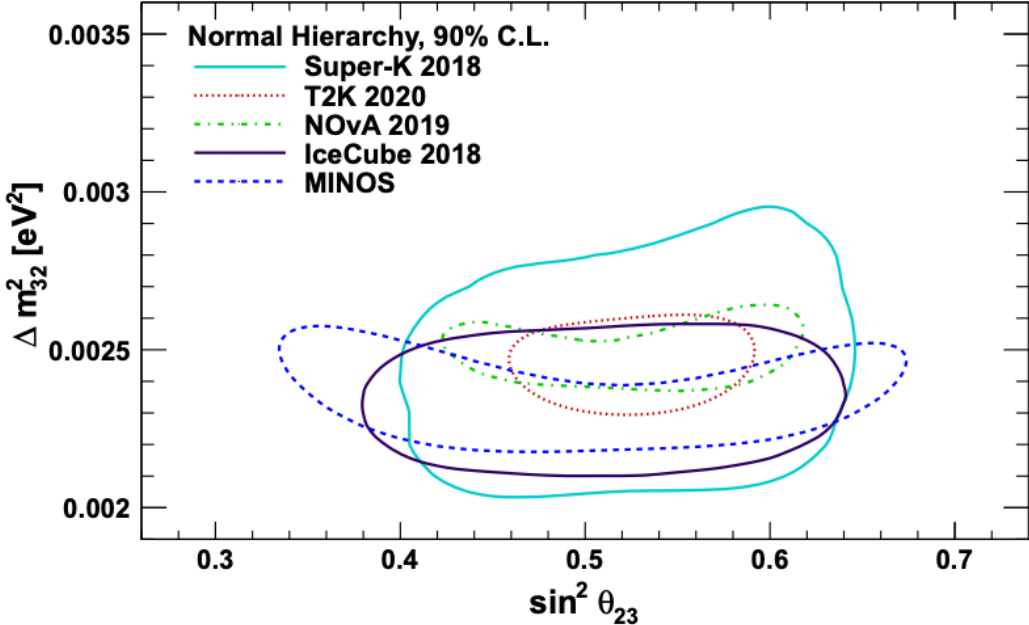


**Figure 1.6:** Constraints on the atmospheric oscillation parameters,  $\sin^2(\theta_{23})$  and  $\Delta m_{23}^2$ , from atmospheric and long baseline experiments: SK [50], T2K [51], NO $\nu$ A [52], IceCube [53] and MINOS [54]. Figure taken from [55].

where  $R(\vec{x})$  is the event rate of neutrinos at position  $\vec{x}$ ,  $\Phi(E_\nu)$  is the flux of neutrinos with energy  $E_\nu$ ,  $\sigma(E_\nu)$  is the cross-section of the neutrino interaction and  $\epsilon(\vec{x})$  is the efficiency of the detector. In order to leverage the most out of an accelerator neutrino experiment, the flux and cross-section systematics need to be constrained. This is typically done via the use of a “near detector”, situated at a baseline of  $O(1)$ km. This detector observes the unoscillated neutrino flux and constrains the parameters used within the flux and cross-section model.

The first accelerator experiments to precisely measure oscillation parameters were MINOS [58] and K2K [59]. These experiments confirmed the  $\nu_\mu \rightarrow \nu_\mu$  oscillations seen in atmospheric neutrino experiments by finding consistent mixing parameter values for  $\sin^2(\theta_{23})$  and  $\Delta m_{23}^2$ . The current generation of accelerator neutrino experiments, T2K and NO $\nu$ A extended this field by observing  $\bar{\nu}_\mu \rightarrow \bar{\nu}_e$  and lead the sensitivity to atmospheric mixing parameters as seen in Figure 1.6 [60]. The two experiments differ in their peak neutrino energy, baseline, and detection technique. The NO $\nu$ A experiment is situated at a baseline of 810km from the NuMI beamline which delivers 2GeV neutrinos. The T2K neutrino beam is peaked around 0.6GeV and propagates 295km. The NO $\nu$ A experiment also uses functionally identical detectors (near and far) which allow the approximate cancellation of detector systematics whereas T2K uses a plastic scin-

<sup>384</sup> tillator technique at the near detector and a water Cherenkov far detector. The future  
<sup>385</sup> generation experiments DUNE [61] and Hyper-Kamiokande [62] will succeed these  
<sup>386</sup> experiments as the high-precision era of neutrino oscillation parameter measurements  
<sup>387</sup> develops.

<sup>388</sup> Several anomalous results have been observed in the LSND [9] and MiniBooNE [10]  
<sup>389</sup> detectors which were designed with purposefully short baselines. Parts of the neu-  
<sup>390</sup> trino community attributed these results to oscillations induced by a fourth “sterile”  
<sup>391</sup> neutrino [63] but several searches in other experiments, MicroBooNE [64] and KAR-  
<sup>392</sup> MEN [65], found no hints of additional neutrino species. The solution to the anomalous  
<sup>393</sup> results are still being determined.

### <sup>394</sup> 1.3.4 Reactor Neutrinos

<sup>395</sup> As illustrated in the first discovery of neutrinos (section 1.1), nuclear reactors are a very  
<sup>396</sup> useful man-made source of electron antineutrinos. For reactors that use low-enriched  
<sup>397</sup> uranium  $^{235}\text{U}$  as fuel, the antineutrino flux is dominated by the  $\beta$ -decay fission of  $^{235}\text{U}$ ,  
<sup>398</sup>  $^{238}\text{U}$ ,  $^{239}\text{Pu}$  and  $^{241}\text{Pu}$  [66] as illustrated in Figure 1.7.

<sup>399</sup> Due to their low energy, reactor electron antineutrinos predominantly interact  
<sup>400</sup> via the inverse  $\beta$ -decay (IBD) interaction. The typical signature contains two signals  
<sup>401</sup> delayed by  $O(200)\mu\text{s}$ ; firstly the prompt photons from positron annihilation, and  
<sup>402</sup> secondly the photons emitted ( $E_{tot}^\gamma = 2.2\text{MeV}$ ) from de-excitation after neutron capture  
<sup>403</sup> on hydrogen. Searching for both signals improves the detector’s ability to distinguish  
<sup>404</sup> between background and signal events [68]. Recently, SK included gadolinium dopants  
<sup>405</sup> into the ultra-pure water to increase the energy released from the photon cascade to  
<sup>406</sup>  $\sim 8\text{MeV}$  and reduce the time of the delayed signal to  $\sim 28\mu\text{s}$ .

<sup>407</sup> There are many short baseline experiments ( $L \sim O(1)\text{km}$ ) that have measured  
<sup>408</sup> the  $\sin^2(\theta_{13})$  and  $\Delta m_{23}^2$  oscillation parameters. Daya Bay [69], RENO [70] and Double  
<sup>409</sup> Chooz [71] have all provided precise measurements, with the first discovery of a  
<sup>410</sup> non-zero  $\theta_{13}$  made by Daya Bay and RENO (and complimented by T2K [71]). The  
<sup>411</sup> constraints on  $\sin^2(\theta_{13})$  by the reactor experiments lead the field and are often used  
<sup>412</sup> as external inputs to accelerator neutrino experiments to improve their sensitivity to  
<sup>413</sup>  $\delta_{CP}$  and mass hierarchy determination. JUNO-TAO [72], a small collaboration within  
<sup>414</sup> the larger JUNO experiment, is a next-generation reactor experiment that aims to  
<sup>415</sup> precisely measure the isotopic antineutrino yields from the different fission chains.

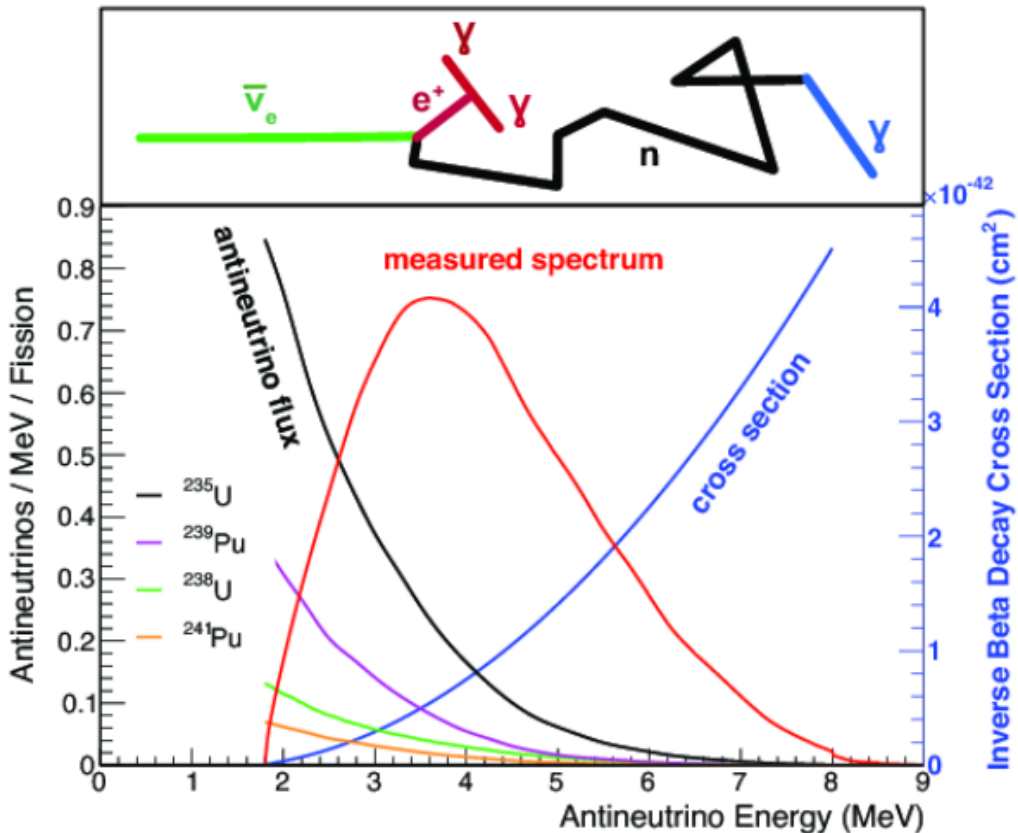


**Figure 1.7:** Reactor electron antineutrino fluxes for  $^{235}\text{U}$  (Black),  $^{238}\text{U}$  (Green),  $^{239}\text{Pu}$  (Purple), and  $^{241}\text{Pu}$  (Orange) isotopes. The inverse  $\beta$ -decay cross-section (Blue) and corresponding measurable neutrino spectrum (Red) are also given. Top panel: Schematic of Inverse  $\beta$ -decay interaction including the eventual capture of the emitted neutron. This capture emits a  $\gamma$ -ray which provides a second signal of the event. Taken from [67].

<sup>416</sup> Alongside this, it aims to explain the ‘5MeV excess’ [73–75] by conducting a search for  
<sup>417</sup> sterile neutrinos with a mass scale of around 1eV.

<sup>418</sup> Kamland [76] is the only experiment to have observed reactor neutrinos using a  
<sup>419</sup> long baseline (flux weighted averaged baseline of  $L \sim 180\text{km}$ ) which allows it to have  
<sup>420</sup> sensitivity to  $\Delta m_{12}^2$ . Combined with the SK solar neutrino experiment, the combined  
<sup>421</sup> analysis puts the most stringent constraint on  $\Delta m_{12}^2$  [77] which is used as a prior  
<sup>422</sup> uncertainty within accelerator neutrino experiments.

## <sup>423</sup> Chapter 2

# <sup>424</sup> T2K and SK Experiment Overview

<sup>425</sup> As the successor of the Kamiokande experiment, the Super-Kamiokande (SK) collaboration has been leading atmospheric neutrino oscillation analyses for over two decades.  
<sup>426</sup> The detector has provided some of the strongest constraints on proton decay limits and  
<sup>427</sup> as well as the first precise measurements of the  $\Delta m_{23}^2$  and  $\sin^2(\theta_{23})$  neutrino oscillation  
<sup>428</sup> parameters. Despite this, the ability of the detector to low-energy neutrino events  
<sup>429</sup> has been significantly improved with the recent gadolinium doping of the ultra-pure  
<sup>430</sup> water target. section 2.1 describes the history, detection technique, and operation of  
<sup>431</sup> the SK detector.

<sup>433</sup> The Tokai-to-Kamioka (T2K) experiment was one of the first long-baseline experiments to use both neutrino and antineutrino beams to precisely measure the  
<sup>434</sup> charge parity violation within the neutrino sector. With the SK detector observing  
<sup>435</sup> the oscillated neutrino flux, the T2K experiment observed the first hints of a non-zero  
<sup>436</sup>  $\sin^2(\theta_{13})$  measurement and continues to lead the field with the constraints it provides  
<sup>437</sup> on  $\sin^2(\theta_{13})$ ,  $\sin^2(\theta_{23})$ ,  $\Delta m_{23}^2$  and  $\delta_{CP}$ . section 2.2 documents the techniques which T2K  
<sup>438</sup> uses in generating its neutrino beam as well as the ‘near-detector’ used to constrain  
<sup>439</sup> the flux and cross-section parameters invoked within the systematic models.

## <sup>441</sup> 2.1 The Super-Kamiokande Experiment

<sup>442</sup> The SK experiment began taking data in 1996 [78] and has had many modifications  
<sup>443</sup> throughout its lifespan. There have been seven defined periods of data taking as  
<sup>444</sup> noted in Table 2.1. Data taking began in SK-I which ran for five years. Between the  
<sup>445</sup> SK-I and SK-II periods, a significant proportion of the PMTs were damaged during  
<sup>446</sup> maintenance. Those that survived were equally distributed throughout the detector  
<sup>447</sup> in the SK-II era, which resulted in a reduced photo-coverage. From SK-III onwards,  
<sup>448</sup> repairs to the detector meant the full suite of PMTs was operational. Before the  
<sup>449</sup> start of SK-IV, the data acquisition and electronic systems were upgraded. Between  
<sup>450</sup> SK-IV and SK-V, a significant effort was placed into tank open maintenance and

451 repair/replacement of defective PMTs, a task for which the author of this thesis was  
 452 required. Consequently, the detector conditions were significantly different between  
 453 the two operational periods. SK-VI saw the start of the 0.01% gadolinium doped  
 454 water. SK-VII, which started during the writing of this thesis, has increased the  
 455 gadolinium concentration to 0.03% for continued operation. [DB: Link to Linyan's talk from Nu2022.](#)

Period	Start Date	End Date	Live-time (days)
I	April 1996	July 2001	1489.19
II	October 2002	October 2005	798.59
III	July 2006	September 2008	518.08
IV	September 2008	May 2018	3244.4
V	January 2019	July 2020	461.02
VI	July 2020	May 2022	583.3
VII	May 2022	Ongoing	N/A

**Table 2.1:** The various SK periods and respective live-time. The SK-VI live-time is calculated until 1<sup>st</sup> April 2022. SK-VII started during the writing of this thesis.

### 457 2.1.1 The SK Detector

458 The basic structure of the Super-Kamiokande (SK) detector is a cylindrical tank with a  
 459 diameter 39.3m and height 41.1m filled with ultrapure water [79]. A diagram of the  
 460 significant components of the SK detector is illustrated in Figure 2.1. The SK detector  
 461 is situated in the Kamioka mine in Gifu, Japan. The mine is underground with roughly  
 462 1km rock overburden (2.7km water equivalent overburden) [80]. At this depth, the  
 463 rate of cosmic ray muons is significantly decreased to a value of  $\sim 2\text{Hz}$ . The top of  
 464 the tank is covered with stainless steel which is designed as a working platform for  
 465 maintenance, calibration, and location for high voltage and data acquisition electronics.

466 A smaller cylindrical structure (36.2m diameter, 33.8m height) is situated inside the  
 467 tank, with an approximate 2m gap between this structure and the outer tank wall. The  
 468 purpose of this structure is to support the photomultiplier tubes (PMTs). The volume  
 469 inside and outside the support structure is referred to as the inner detector (ID) and  
 470 outer detector (OD), respectively. In the SK-IV era, the ID and OD are instrumented  
 471 by 11,129 50cm and 1,885 20cm PMTs respectively [79]. The ID contains a 32kton  
 472 mass of water. Many analyses performed at SK use a “fiducial volume” defined by the

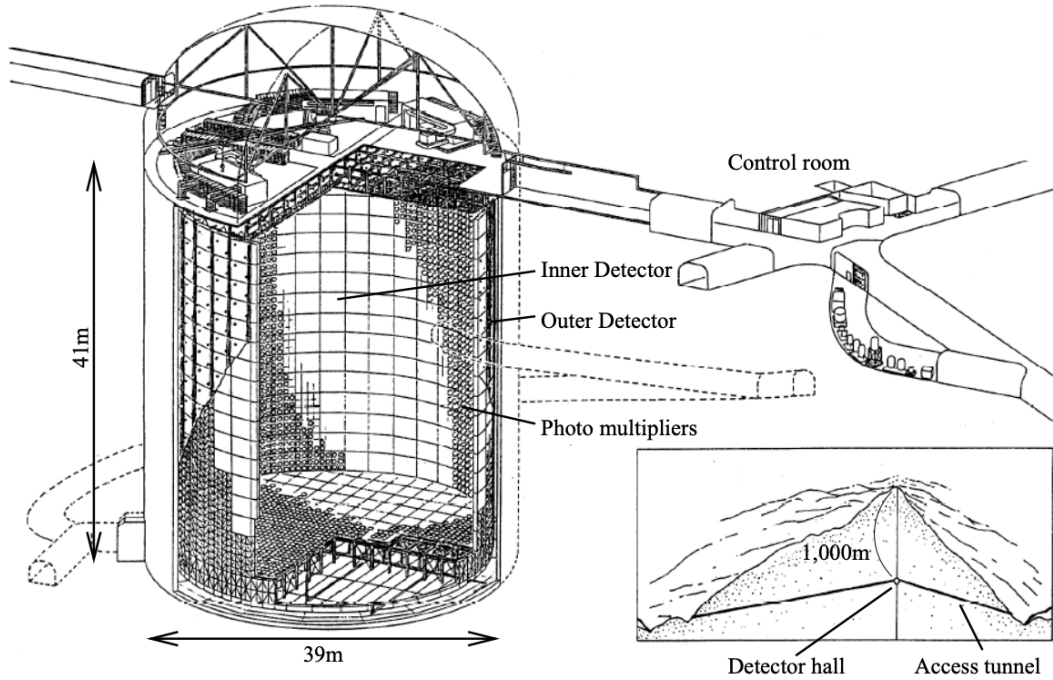


**Figure 2.1:** A schematic diagram of the Super-Kamiokande Detector. Taken from [81].

473 volume of water inside the ID excluding some distance to the ID wall. This reduces the  
 474 volume of the detector which is sensitive to neutrino events but reduces radioactive  
 475 backgrounds and allows for better reconstruction performance. The nominal fiducial  
 476 volume is defined as the area contained inside 2m from the ID wall for a total of  
 477 22.5kton water [82].

478 The two regions of the detector (ID and OD) are optically separated with opaque  
 479 black plastic. The purpose of this is to determine whether a track entered or exited  
 480 the ID. This allows cosmic ray muons and partially contained events to be tagged and  
 481 separated from neutrino events entirely contained within the ID. This black plastic is  
 482 also used to cover the area between the ID PMTs to reduce photon reflection from the  
 483 ID walls. Opposite to this, the OD is lined with a reflective material to allow photons to  
 484 reflect around inside the OD until collected by one of the PMTs. Furthermore, each OD  
 485 PMT is backed with  $50 \times 50\text{cm}$  plates of wavelength shifting acrylic which increases  
 486 the efficiency of light collection [80].

487 In the SK-IV data-taking period, the photocathode coverage of the detector, or the  
 488 fraction of the ID wall instrumented with PMTs, is  $\sim 40\%$  [80]. The PMTs have a  
 489 quantum efficiency (the ratio of detected electrons to incident photons) of  $\sim 21\%$  for  
 490 photons with wavelengths of  $360\text{nm} < \lambda < 390\text{nm}$ . The proportion of photoelectrons

491 that produce a signal in the dynode of a PMT, termed the collection efficiency, is  
492  $> 70\%$  [80]. The PMTs used within SK are most sensitive to photons with wavelength  
493  $300\text{nm} \leq \lambda \leq 600\text{nm}$  [80]. One disadvantage of using PMTs as the detection media  
494 is that the Earth's geomagnetic field can modify its response. Therefore, a set of  
495 compensation coils is built around the inner surface of the detector to mitigate this  
496 effect [83].

497 As mentioned, the SK detector is filled with ultrapure water, which in a perfect  
498 world would contain no impurities. However, bacteria and organic compounds can  
499 significantly degrade the water quality. This decreases the attenuation length which  
500 reduces the total number of photons that hit a PMT. To combat this, a sophisticated  
501 water treatment system has been developed [80, 84]. UV lights, mechanical filters, and  
502 membrane degasifiers are used to reduce the bacteria, suspended particulates, and  
503 radioactive materials from the water. The flow of water within the tank is also critical  
504 as it can remove stagnant bacterial growth or build-up of dust on the surfaces within  
505 the tank. Gravity drifts impurities in the water towards the bottom of the tank which,  
506 if left uncontrolled, can create asymmetric water conditions between the top and  
507 bottom of the tank. Typically, the water entering the tank is cooled below the ambient  
508 temperature of the tank to control convection and inhibit bacteria growth. Furthermore,  
509 the dark noise hits within PMTs is sensitive to the PMT temperature [85] so controlling  
510 the temperature gradients within the tank is beneficial for stable measurements.

511 SK-VI is the first phase of the SK experiment to use gadolinium dopants within  
512 the ultrapure water DB: [Link to Linyan's talk at Nu2022](#). As such, the SK water  
513 system had to be replaced to avoid removing the gadolinium concentrate from the  
514 ultrapure water [86]. For an inverse  $\beta$ -decay (IBD) interaction in a water target, the  
515 emitted neutron is thermally captured on hydrogen. This process releases 2.2MeV  $\gamma$   
516 rays which are difficult to detect due to Compton scattered electrons from a  $\gamma$  ray of  
517 this energy is very close to the Cherenkov threshold, limiting the number of photons  
518 produced. Thermal capture of neutrons on gadolinium generates  $\gamma$  rays with higher  
519 energy meaning they are more easily detected. SK-VI has 0.01% Gd loading (0.02%  
520 gadolinium sulphate by mass) which causes  $\approx 50\%$  of neutrons emitted by IBD to  
521 be captured on gadolinium [87, 88]. Whilst predominantly useful for low energy  
522 analyses, Gd loading allows better  $\nu/\bar{\nu}$  separation for atmospheric neutrino event  
523 selections [89]. Efforts are currently in place to increase the gadolinium concentrate to  
524 0.03% for  $\approx 75\%$  neutron capture efficiency on gadolinium DB: [Link to Mark's talk at](#)  
525 [Nu2022](#). The final stage of loading targets 0.1% concentrate.

### 526 2.1.2 Calibration

527 The calibration of the SK detector is documented in [79] and summarised below. The  
528 analysis presented within this thesis is dependent upon ‘high energy events’ (Charged  
529 particles with  $O(> 100)\text{MeV}$  momenta). These are events that are expected to generate  
530 a larger number of photons such that each PMT will be hit with multiple photons.  
531 The reconstruction of these events depends upon the charge deposited within each  
532 PMT and the timing response of each individual PMT. Therefore, the most relevant  
533 calibration techniques to this thesis are outlined.

534 Before installation, 420 PMTs were calibrated to have identical charge responses  
535 and then distributed throughout the tank in a cross-shape pattern (As illustrated by  
536 Figure 2.2). These are used as a standardised measure for the rest of the PMTs installed  
537 at similar geometric positions within SK to be calibrated against. To perform this  
538 calibration, a xenon lamp is located at the center of the SK tank which flashes uniform  
539 light at 1Hz. This allows for geometrical effects, water quality variation, and timing  
540 effects to be measured in-situ throughout normal data-taking periods.

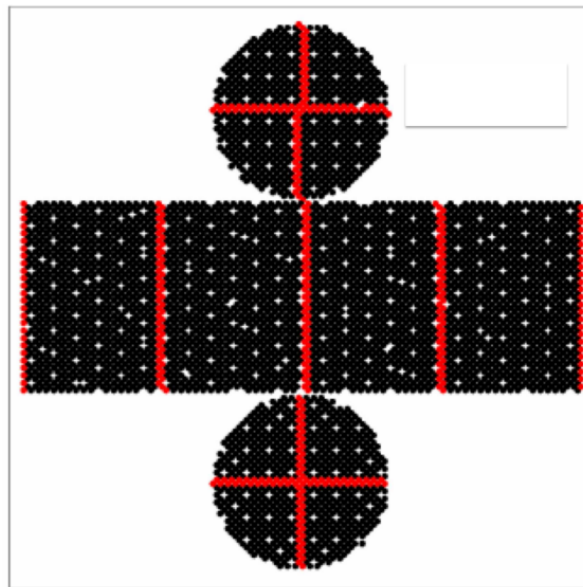


**Figure 2.2:** The location of “standard PMTs” (red) inside the SK detector. Taken from [79].

541 When specifically performing calibration of the detector (in out-of-data taking  
542 mode), the water in the tank was circulated to avoid top/bottom asymmetric water  
543 quality. Any non-uniformity within the tank significantly affects the PMT hit proba-  
544 bility through scattering or absorption. This becomes a dominant effect for the very

545 low-intensity light sources discussed later which are designed such that only one  
 546 photon is incident upon a given PMT.

547 The “gain” of a PMT is defined as the ratio of the total charge of the signal produced  
 548 compared to the charge of photoelectrons emitted by the photocathodes within the  
 549 PMT. To calibrate the signal of each PMT, the “relative” and “absolute” gain values are  
 550 measured. The relative gain is the variation of gain among each of the PMTs whereas  
 551 the absolute gain is the average gain of all PMTs.

552 The relative gain is calibrated as follows. A laser is used to generate two measure-  
 553 ments; a high-intensity flash that illuminates every PMT with a sufficient number of  
 554 photons, and a low-intensity flash in which only a small number of PMTs collect light.  
 555 The first measurement creates an average charge,  $Q_{obs}(i)$  on PMT  $i$ , whereas the second  
 556 measurement ensures that each hit PMT only generates a single photoelectron. For the  
 557 low-intensity measurement, the number of times each PMT records a charge larger  
 558 than 1/4 photoelectrons,  $N_{obs}(i)$ , is counted. The values measured can be expressed as

$$\begin{aligned} Q_{obs}(i) &\propto I_H \times f(i) \times \epsilon(i) \times G(i), \\ N_{obs}(i) &\propto I_L \times f(i) \times \epsilon(i), \end{aligned} \quad (2.1)$$

559 Where  $I_H$  and  $I_L$  is the intensity of the high and low flashes,  $f(i)$  is the acceptance  
 560 efficiency of the  $i^{\text{th}}$  PMT,  $\epsilon(i)$  is the product of the quantum and collection efficiency  
 561 of the  $i^{\text{th}}$  PMT and  $G(i)$  is the gain of the  $i^{\text{th}}$  PMT. The relative gain for each PMT can  
 562 determined by taking the ratio of these quantities.

563 The absolute gain calibration is performed by observing fixed energy  $\gamma$ -rays of  
 564  $E_\gamma \sim 9\text{MeV}$  emitted isotropically from neutron capture on a NiCf source situated at  
 565 the center of the detector. This generates a photon yield of about 0.004 photoelec-  
 566 trons/PMT/event, meaning that  $> 99\%$  of PMT signals are generated from single  
 567 photoelectrons. A charge distribution is generated by performing this calibration over  
 568 all PMTs, and the average value of this distribution is taken to be the absolute gain  
 569 value.

570 As mentioned in subsection 2.1.1, the average quantum and collection efficiency  
 571 for the SK detector is  $\sim 21\%$  and  $> 70\%$  respectively. However, these values do differ  
 572 between each PMT and need to be calibrated accordingly. Consequently, the NiCf  
 573 source is also used to calibrate the “quantum  $\times$  collection” efficiency (denoted “QE”)

574 value of each PMT. The NiCf low-intensity source is used as the PMT hit probability  
575 is proportional to the QE ( $N_{obs}(i) \propto \epsilon(i)$  in Equation 2.1). A Monte Carlo prediction  
576 which includes photon absorption, scattering, and reflection is made to estimate the  
577 number of photons incident on each PMT and the ratio of the number of predicted  
578 to observed hits is calculated. The difference is attributed to the QE efficiency of that  
579 PMT. This technique is extended to calculate the relative QE efficiency by normalizing  
580 the average of all PMTs which removes the dependence on the light intensity.

581 Due to differing cable lengths and readout electronics, the timing response between  
582 a photon hitting the PMT and the signal being captured by the data acquisition can be  
583 different between each PMT. Due to threshold triggers (Described in subsection 2.1.3),  
584 the time at which a pulse reaches a threshold is dependent upon the size of the pulse.  
585 This is known as the ‘time-walk’ effect and also needs to be accounted for in each PMT.  
586 To calibrate the timing response, a pulse of light with width 0.2ns is emitted into the  
587 detector through a diffuser Two-dimensional distributions of time and pulse height  
588 (or charge) are made for each PMT and are used to calibrate the timing response. This  
589 is performed in-situ whilst data taking with the light source pulsing at 0.03Hz.

590 The top/bottom water quality asymmetry is measured using the NiCf calibration  
591 data and cross-referencing these results to the “standard PMTs”. The water attenuation  
592 length is continuously measured by the rate of vertically-downgoing cosmic-ray  
593 muons which enter via the top of the tank.

### 594 2.1.3 Data Acquisition and Triggering

595 Dark noise is the phenomenon where a PMT registers a pulse that is consistent with a  
596 single photoelectron emitted from photon detection despite the PMT being in complete  
597 darkness. This is predominately caused by two processes. Firstly there is intrinsic  
598 dark noise which is where photoelectrons gain enough thermal energy to be emitted  
599 from the photocathode, and secondly, the radioactive decay of contaminants inside the  
600 structure of the PMT. Typical dark noise rate for PMTs used within SK are  $O(3)\text{kHz}$  [80]  
601 which equates to about 12 dark noise hits per 220ns [90]. This is lower than the  
602 expected number of photons generated for a ‘high energy event’ (As described in  
603 subsection 2.1.4) but instability in this value can cause biases in reconstruction.

604 The analysis presented in this thesis only uses the SK-IV period of the SK exper-  
605 iment so this subsection focuses on the relevant points of the data acquisition and

606 triggering systems to that SK period. The earlier data acquisition and triggering  
607 systems are documented in [91, 92].

608 Before the SK-IV period started, the existing front-end electronics were replaced  
609 with “QTC-Based Electrons with Ethernet, QBEE” systems [93]. When the QBEE  
610 observes a signal above a 1/4 photoelectron threshold, the charge-to-time (QTC)  
611 converter generates a rectangular pulse. The start of the rectangular pulse indicates  
612 the time at which the analog photoelectron signal was received and the width of the  
613 pulse indicates the total charge integrated throughout the signal. This is then digitized  
614 by time-to-digital converters and sent to the “front-end” PCs. The digitized signal  
615 from every QBEE is then chronologically ordered and sent to the “merger” PCs. It is  
616 the merger PCs that apply the software trigger. Any triggered events are passed to the  
617 “organizer” PC. This sorts the data stream of multiple merger PCs into chronologically  
618 ordered events which are then saved to disk. The schematic of data flow from PMTs to  
619 disk is illustrated in Figure 2.3.

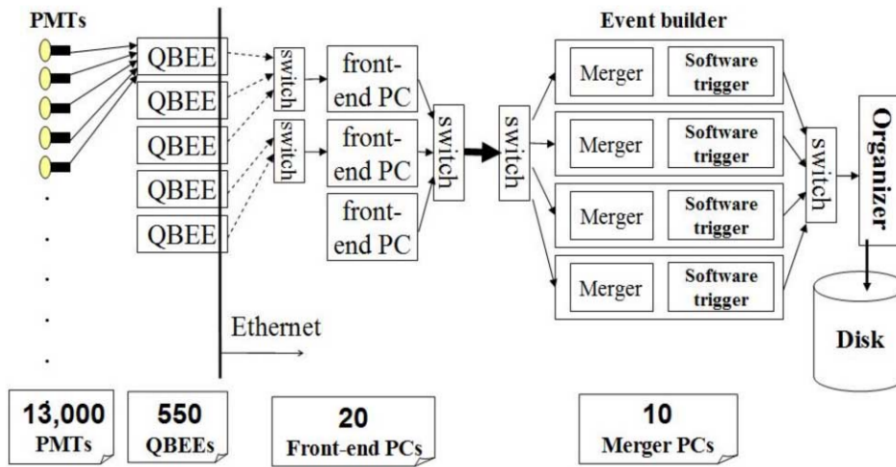


**Figure 2.3:** Schematic view of the data flow through the data acquisition and online system.  
 Taken from [94].

620 The software trigger (described in [95]) operates by determining the number of  
621 PMT hits within a 200ns sliding window,  $N_{200}$ , coincides with the maximum time that  
622 a Cherenkov photon would take to traverse the length of the SK tank [92]. For lower  
623 energy events that generate fewer photons, this technique is useful for eliminating  
624 background processes like dark noise and radioactive decay which would be expected  
625 to separate in time. When the value of  $N_{200}$  exceeds some threshold, a software trigger  
626 is issued. There are several trigger thresholds used within the SK-IV period which are  
627 detailed in Table 2.2. If one of these thresholds is met, the PMT hits within an extended

time window are also read out and saved to disk. In the special case of an event that exceeds the SHE trigger but does not exceed the OD trigger, the AFT trigger looks for delayed coincidences of 2.2MeV gamma rays emitted from neutron capture in a  $535\mu\text{s}$  window after the SHE trigger. A similar but more complex “Wideband Intelligent Trigger (WIT)” has been deployed and is described in [90].

Trigger	Acronym	Condition	Extended time window ( $\mu\text{s}$ )
Super Low Energy	SLE	>34/31 hits	1.3
Low Energy	LE	>47 hits	40
High Energy	HE	>50 hits	40
Super High Energy	SHE	>70/58 hits	40
Outer Detector	OD	>22 hits in OD	N/A

**Table 2.2:** The trigger thresholds and extended time windows saved around an event which were utilised throughout the SK-IV period. The exact thresholds can change and the values listed here represent the thresholds at the start and end of the SK-IV period.

### 2.1.4 Cherenkov Radiation

Cherenkov light is emitted from any highly energetic charged particle traveling with relativistic velocity,  $\beta$ , greater than the local speed of light in a medium [96]. Cherenkov light is formed at the surface of a cone with characteristic pitch angle,

$$\cos(\theta) = \frac{1}{\beta n}. \quad (2.2)$$

where  $n$  is the refractive index of the medium. Consequently, the Cherenkov momentum threshold,  $P_{thres}$ , is dependent upon the mass,  $m$ , of the charged particle moving through the media,

$$P_{thres} = \frac{m}{\sqrt{n^2 - 1}} \quad (2.3)$$

For water, where  $n = 1.33$ , the Cherenkov threshold momentum and energy for various particles are given in Table 2.3. In contrast,  $\gamma$ -rays are detected indirectly via

the combination of photons generated by Compton scattering and pair production. The threshold for detection in the SK detector is typically higher than the threshold for photon production. This is due to the fact that the attenuation of photons in the water means that typically  $\sim 75\%$  of Cherenkov photons reach the ID PMTs. Then the collection and quantum efficiencies described in subsection 2.1.1 result in the number of detected photons being lower than the number of photons which reach the PMTs.

Particle	Threshold Momentum (MeV)	Threshold Energy (MeV)
Electron	0.5828	0.7751
Muon	120.5	160.3
Pion	159.2	211.7
Proton	1070.0	1423.1

**Table 2.3:** The threshold momentum and energy for a particle to generate Cherenkov light in ultrapure water, as calculated in Equation 2.2 in ultrapure water which has refractive index  $n = 1.33$ .

The Frank-Tamm equation [97] describes the relationship between the number of Cherenkov photons generated per unit length,  $dN/dx$ , the wavelength of the photons generated,  $\lambda$ , and the relativistic velocity of the charged particle,

$$\frac{d^2N}{dxd\lambda} = 2\pi\alpha \left(1 - \frac{1}{n^2\beta^2}\right) \frac{1}{\lambda^2}. \quad (2.4)$$

where  $\alpha$  is the fine structure constant. For a 100MeV momentum electron, approximately 330 photons will be produced per centimeter in the  $300\text{nm} \leq \lambda \leq 700\text{nm}$  region which the ID PMTs are most sensitive to [80].

## 2.2 The Tokai to Kamioka Experiment

The Tokai to Kamioka (T2K) experiment is a long-baseline neutrino oscillation experiment located in Japan. Proposed in the early 2000s [98, 99] to replace K2K [100], T2K was designed to observe electron neutrino appearance whilst precisely measuring the oscillation parameters associated with muon neutrino disappearance [101]. The experiment consists of a neutrino beam generated at the Japan Proton Accelerator Research Complex (J-PARC), a suite of near detectors situated 280m from the beam

target, and the Super Kamiokande far detector positioned at a 295km baseline. The cross-section view of the T2K experiment is drawn in Figure 2.4.

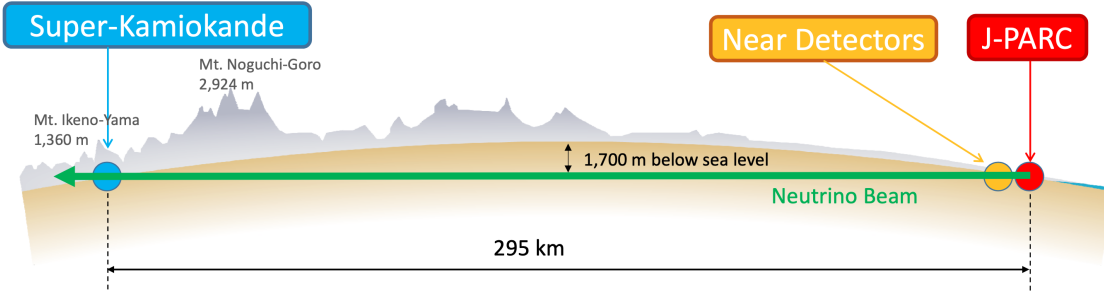


**Figure 2.4:** The cross-section view of the Tokai to Kamioka experiment illustrating the beam generation facility at J-PARC, the near detector situated at a baseline of 280m and the Super Kamiokande far detector situated 295km from the beam target.

The T2K collaboration makes world-leading measurements of the  $\sin^2(\theta_{23})$ ,  $\Delta m_{23}^2$ , and  $\delta_C$  oscillation parameters. Improvements in the precision and accuracy of parameter estimates are still being made by including new data samples and developing the models which describe the neutrino interactions and detector responses DB: [Link to Christophe's slides from Nu2022](#). Electron neutrino appearance was first observed at T2K in 2014 [102] which accompanied a  $7.3\sigma$  significance of a non-zero  $\sin^2(\theta_{13})$  measurement.

The near detectors provide constraints on the beam flux and cross-section model parameters used within the fit by observing the unoscillated neutrino beam. There are a host of detectors situated in the near detector hall (As illustrated in Figure 2.5); ND280 (subsection 2.2.2), INGRID (subsection 2.2.3), NINJA [103], WAGASCI [104], and Baby-MIND [105]. The latter three are not currently used within the oscillation analysis presented within this thesis.

Whilst this thesis presents the ND280 in terms of its purpose for the oscillation analysis, the detector can also make many cross-section measurements at neutrino energies of  $O(1)\text{GeV}$  for the different targets within the detector [106, 107]. These measurements are of equal importance as they can lead the way in determining the model parameters used in the interaction models for the future high-precision era of neutrino physics.

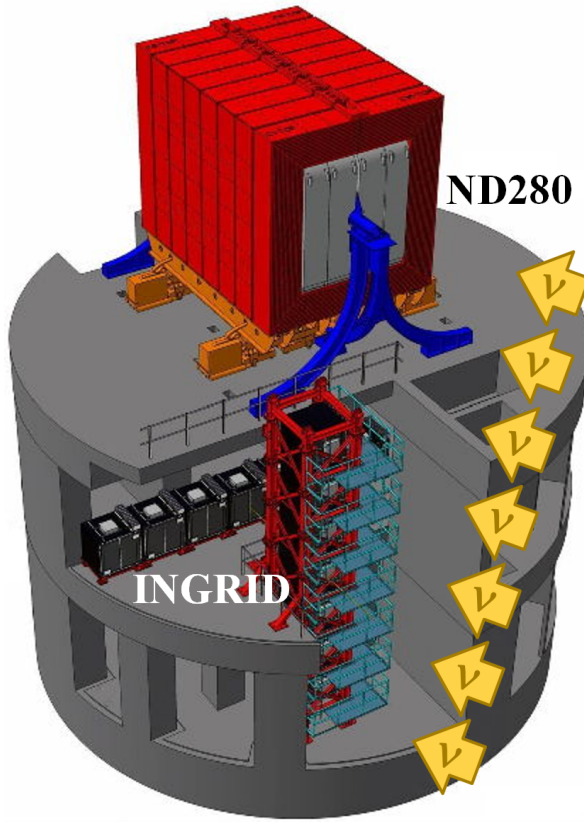
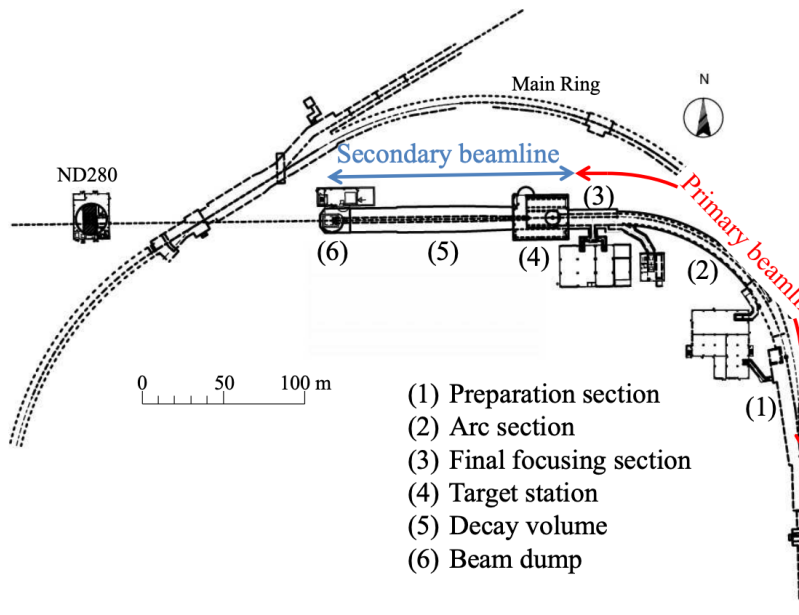


**Figure 2.5:** The near detector suite for the T2K experiment showing the ND280 and INGRID detectors. The distance between the detectors and the beam target is 280m.

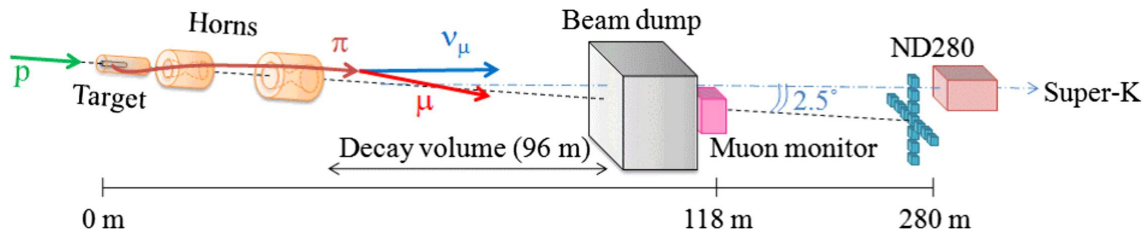
### 682 2.2.1 The Neutrino Beam

683 The neutrino beam used within the T2K experiment is described in [57, 108] and  
 684 summarised below. The accelerating facility at J-PARC is composed of two sections; the  
 685 primary and secondary beamlines. Figure 2.6 illustrates a schematic of the beamline,  
 686 focusing mostly on the components of the secondary beamline. The primary beamline  
 687 has three accelerators that progressively accelerate protons; a linear accelerator, a rapid-  
 688 cycling synchrotron, and the main-ring (MR) synchrotron. Once fully accelerated by  
 689 the MR, the protons have a kinetic energy of 30GeV. Eight bunches of these protons,  
 690 separated by 500ns, are extracted per “spill” from the MR and directed towards a  
 691 graphite target (A rod of length 91.4cm and diameter 2.6cm). Spills are extracted at  
 692 0.5Hz with  $\sim 3 \times 10^{14}$  protons contained per spill.

693 The secondary beamline consists of three main components; the target station, the  
 694 decay volume, and the beam dump. The target station is comprised of the target, beam  
 695 monitors, and three magnetic focusing horns. The proton beam interacts with the  
 696 graphite target to form a secondary beam of mostly pions and kaons. The secondary



(a) Primary and secondary beamline

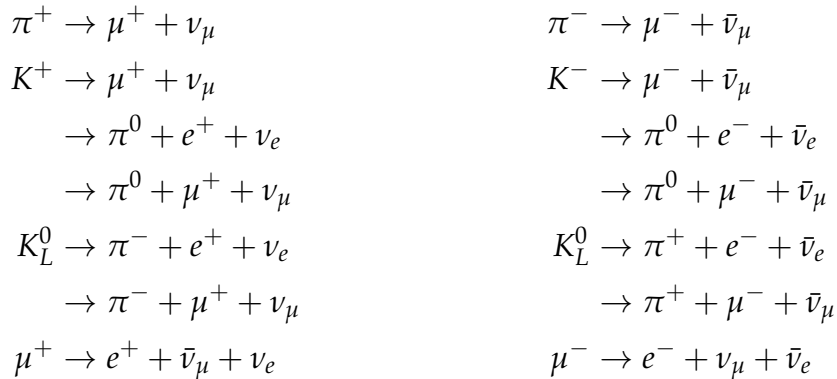


(b) Secondary beamline

**Figure 2.6:** Top panel: Bird's eye view of the most relevant part of primary and secondary beamline used within the T2K experiment. The primary beamline is the main-ring proton synchrotron, kicker magnet, and graphite target. The secondary beamline consists of the three focusing horns, decay volume, and beam dump. Figure taken from [108]. Bottom panel: The side-view of the secondary beamline including the focusing horns, beam dump and neutrino detectors. Figure taken from [109].

beam travels through a 96m long decay volume, generating neutrinos through the following decays [57],

<sup>697</sup> beam travels through a 96m long decay volume, generating neutrinos through the  
<sup>698</sup> following decays [57],



699     The electrically charged component of the secondary beam is focused towards the  
700 far detector by the three magnetic horns. These horns direct charged particles of a  
701 particular polarity towards SK whilst defocusing the oppositely charged particles.  
702 This allows a mostly neutrino or mostly antineutrino beam to be used within the  
703 experiment, denoted as “forward horn current (FHC)” or “reverse horn current (RHC)”  
704 respectively.

705     Figure 2.7 illustrates the different contributions to the FHC and RHC neutrino flux.  
706 The low energy flux is dominated by the decay of pions whereas kaon decay becomes  
707 the dominant source of neutrinos for  $E_\nu > 3\text{GeV}$ . The “wrong-sign” component, which  
708 is the  $\bar{\nu}_\mu$  background in a  $\nu_\mu$  beam, and the intrinsic irreducible  $\nu_e$  background are  
709 predominantly due to muon decay for  $E_\nu < 2\text{GeV}$ . As the antineutrino cross-section is  
710 smaller than the neutrino cross-section, the wrong-sign component is more dominant  
711 in the RHC beam as compared to that in the FHC beam.

712     The beam dump, situated at the end of the decay volume, stops all charged particles  
713 other than highly energetic muons ( $p_\mu > 5\text{GeV}$ ). The MuMon detector monitors the  
714 penetrating muons to determine the beam direction and intensity which is used to  
715 constrain some of the beam flux systematics within the analysis [109, 111].

716     The T2K experiment uses an off-axis beam to narrow the neutrino energy distribution.  
717 This was the first implementation of this technique in a long-baseline neutrino  
718 oscillation experiment after its original proposal [112]. Pion decay,  $\pi \rightarrow \mu + \nu_\mu$ , is a  
719 two-body decay. Consequently, the neutrino energy,  $E_\nu$ , can be determined based on  
720 the pion energy,  $E_\pi$ , and the angle at which the neutrino is emitted,  $\theta$ ,

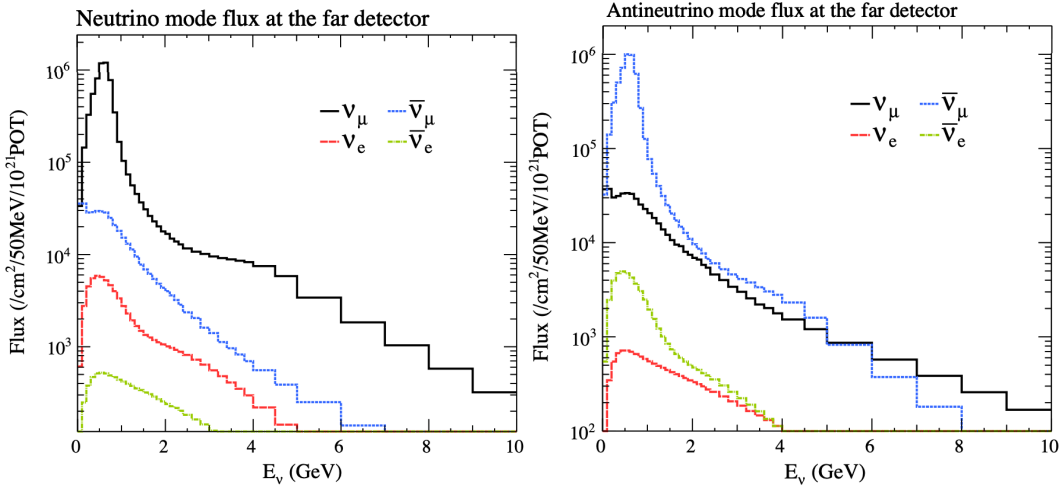


**Figure 2.7:** The Monte Carlo prediction of the energy spectrum for each flavour of neutrino ( $\nu_e$ ,  $\bar{\nu}_e$ ,  $\nu_\mu$  and  $\bar{\nu}_\mu$ ) in the neutrino dominated beam FHC mode (Left) and antineutrino dominated beam RHC mode (Right) expected at SK. Taken from [110].

$$E_\nu = \frac{m_\pi^2 - m_\mu^2}{2(E_\pi - p_\pi \cos(\theta))}, \quad (2.5)$$

where  $m_\pi$  and  $m_\mu$  are the mass of the pion and muon respectively. For a fixed energy pion, the neutrino energy distribution is dependent upon the angle at which the neutrinos are observed from the initial pion beam direction. For the 295km baseline at T2K,  $E_\nu = 0.6\text{GeV}$  maximises the electron neutrino appearance probability,  $P(\nu_\mu \rightarrow \nu_e)$ , whilst minimising the muon disappearance probability,  $P(\nu_\mu \rightarrow \nu_\mu)$ . Figure 2.8 illustrates the neutrino energy distribution for a range of off-axis angles, as well as the oscillation probabilities most relevant to T2K.

## 2.2.2 The Near Detector at 280m

Whilst all the near detectors are situated in the same “pit” located at 280m from the beamline, the “ND280” detector is the off-axis detector which is situated at the same off-axis angle as the Super-Kamiokande far detector. It has two primary functions; firstly it measures the neutrino flux and secondly it counts the event rates of different types of neutrino interactions. Both of these constrain the flux and cross-section systematics invoked within the model for a more accurate prediction of the expected event rate at the far detector.

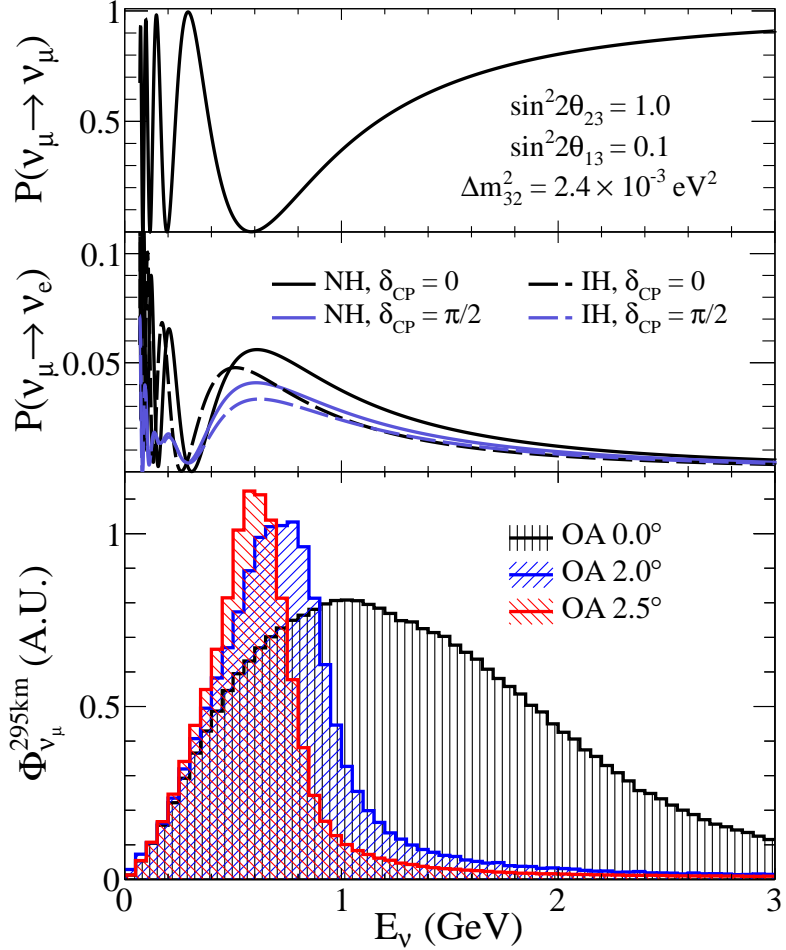


**Figure 2.8:** Top panel: T2K muon neutrino disappearance probability as a function of neutrino energy. Middle panel: T2K electron neutrino appearance probability as a function of neutrino energy. Bottom panel: The neutrino flux distribution for three different off-axis angles (Arbitrary units) as a function of neutrino energy.

As illustrated in Figure 2.9, the ND280 detector consists of several sub-detectors.

The most important part of the detector for this analysis is the tracker region. This is comprised of two time projection chambers (TPCs) sandwiched between three fine grain detectors (FGDs). The FGDs contain both hydrocarbon plastics and water targets for neutrino interactions and provide track reconstruction near the interaction vertex. The emitted charged particles can then propagate into the TPCs which provide particle identification and momentum reconstruction. The FGDs and TPCs are further described in subsubsection 2.2.2.1 and subsubsection 2.2.2.2 respectively. The electromagnetic calorimeter (ECAL) encapsulates the tracker region alongside the  $\pi^0$  detector (P0D). The ECAL measures the deposited energy from photons emitted from interactions within the FGD. The P0D constrains the cross-section of neutral current interactions which generate neutral pions, which is one of the largest backgrounds in

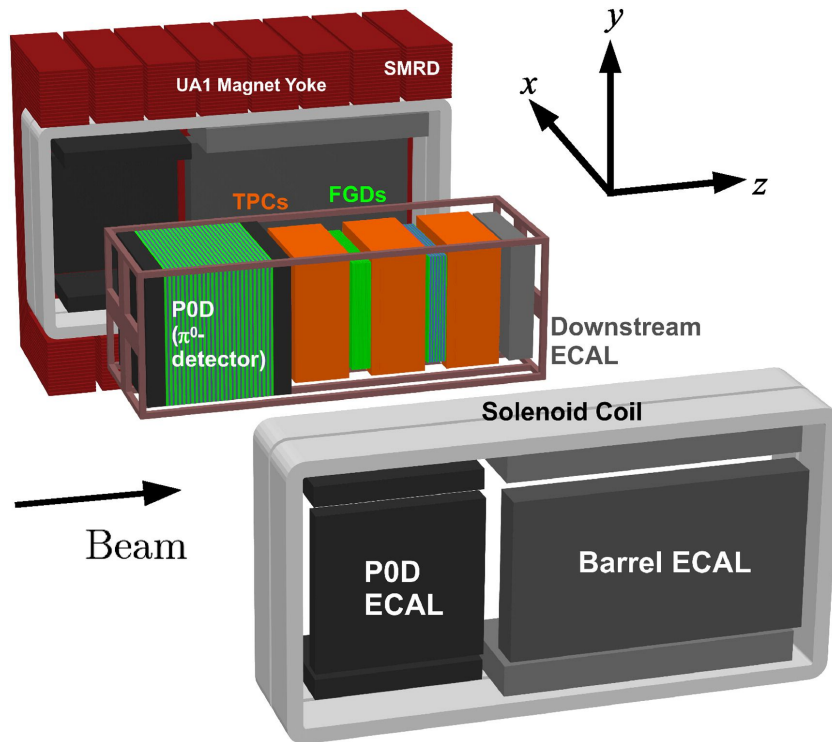


**Figure 2.9:** The components of the ND280 detector. The neutrino beam travels from left to right. Taken from [108].

749 the electron neutrino appearance oscillation channel. The P0D and ECAL detectors  
 750 are detailed in subsubsection 2.2.2.3 and subsubsection 2.2.2.4 respectively. The entire  
 751 detector is located within a large yolk magnet which produces a 0.2T magnetic field.  
 752 This design of the magnet also includes a scintillating detector called the side muon  
 753 range detector (SMRD) which is used to track high-angle muons as well as acting as a  
 754 cosmic veto. The SMRD is described in subsubsection 2.2.2.5.

### 755 2.2.2.1 Fine Grained Detectors

756 The T2K tracker region is comprised of two fine grained detectors (FGD) and three  
 757 Time Projection Chambers (TPC). A detailed description of the FGD design, construc-  
 758 tion, and assembly is found in [113] and summarised below. The FGDs are the primary  
 759 target for neutrino interactions with a mass of 1.1 tonnes per FGD. Alongside this,  
 760 the FGDs are designed to be able to track short-range particles which do not exit the  
 761 FGD. Typically, short-range particles are low momentum and are observed as tracks  
 762 that deposit a large amount of energy per unit length. This means the FGD needs  
 763 good granularity to resolve these particles. The FGDs have the best timing resolution  
 764 ( $\sim 3\text{ns}$ ) of any of the sub-detectors of the ND280 detector. As such, the FGDs are

765 used for time of flight measurements to determine forward going positively charged  
 766 particles from backward going negatively charged particles. Finally, any tracks which  
 767 pass through multiple sub-detectors are required to be track matched to the FGD.

768 Both FDGs are made from square scintillator planes of side length 186cm and width  
 769 2.02cm. Each plane consists of two layers of 192 scintillator bars in an XY orientation.  
 770 A wave-length shift fiber is threaded through the center of each bar and is read out by  
 771 a multi-photon pixel counter (MPPC). FGD1 is the most upstream of the two FDGs  
 772 and contains 15 planes of carbon plastic scintillator which is a common target in  
 773 external neutrino scattering data. As the far detector is a pure water target, 7 of the 15  
 774 scintillator planes in FGD2 have been replaced with a hybrid water-scintillator target.  
 775 Due to the complexity of the nucleus, nuclear effects can not be extrapolated between  
 776 different nuclei. Therefore having the ability to take data on one target which is the  
 777 same as external data and another target which is the same as the far detector target is  
 778 beneficial for reliable model parameter estimates.

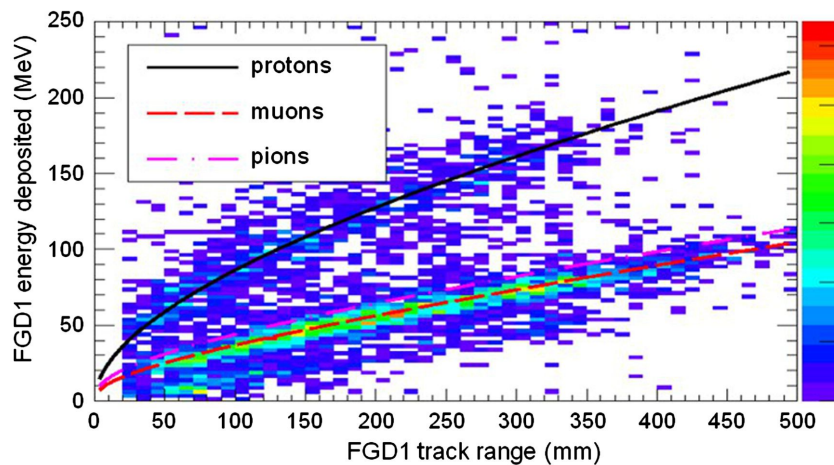


**Figure 2.10:** Comparison of data to Monte Carlo prediction of integrated deposited energy as a function of track length for particles that stopped in FGD1. Taken from [113].

779 The integrated deposited energy is used for particle identification. The FGD  
 780 can distinguish protons from other charged particles by comparing the integrated  
 781 deposited energy from data to Monte Carlo prediction as seen in Figure 2.10.

### 782 2.2.2.2 Time Projection Chambers

783 The majority of particle identification and momentum measurements within ND280  
 784 are provided by three Time Projection Chambers (TPCs) [114]. The TPCs are located

785 on either side of the FGDs. They are located inside of the magnetic field meaning the  
 786 momentum of a charged particle can be determined from the bending of the track.

787 Each TPC module consists of two gas-tight boxes, as shown in Figure 2.11, which  
 788 are made of non-magnetic material. The outer box is filled with CO<sub>2</sub> which acts as  
 789 an electrical insulator between the inner box and the ground. The inner box forms  
 790 the field cage which produces a uniform electric drift field of  $\sim 275\text{V/cm}$  and an  
 791 argon gas mixture. Charged particles moving through this gas mixture ionize the gas  
 792 mixture. The ionised charge is drifted towards micromega detectors which measure  
 793 the ionization charge. The time and position information in the readout allows a  
 794 three-dimensional image of the neutrino interaction.

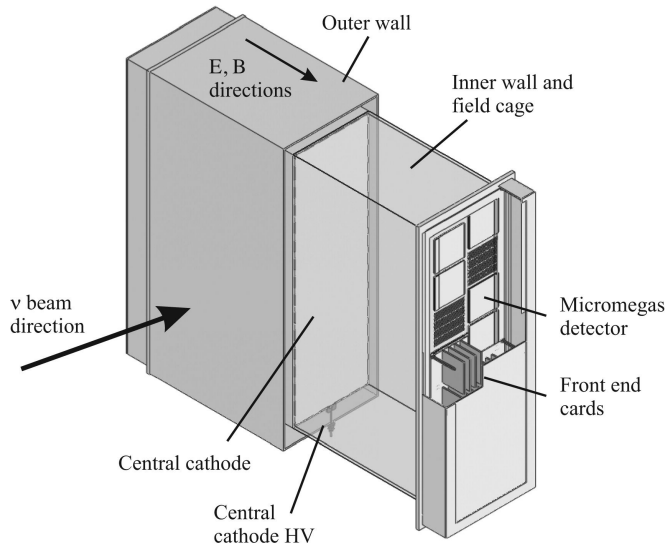
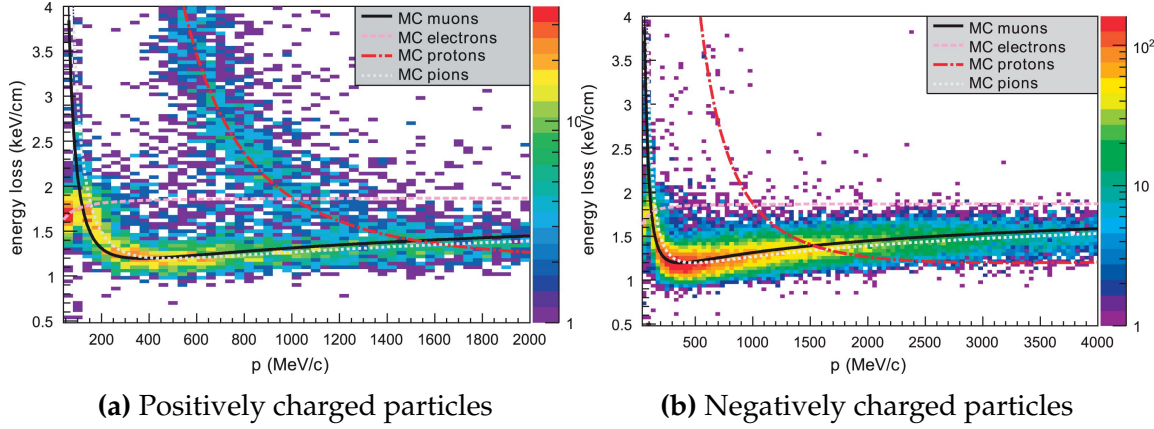


Figure 2.11: Schematic design of a Time Projection Chamber detector. Taken from [114].

795 The particle identification of tracks that pass through the TPCs is performed using  
 796 dE/dx measurements. Figure 2.12 illustrates the data to Monte Carlo distributions  
 797 of the energy lost by a charged particle passing through the TPC as a function of the  
 798 reconstructed particle momentum. The resolution is  $7.8 \pm 0.2\%$  meaning that electrons  
 799 and muons can be distinguished. This allows reliable measurements of the intrinsic  $\nu_e$   
 800 component of the beam.

### 801 2.2.2.3 $\pi^0$ Detector

802 If one of the  $\gamma$ -rays from a  $\pi^0 \rightarrow 2\gamma$  decay is missed at the far detector, the reconstruc-  
 803 tion will determine that event to be electron-like. This is one of the main backgrounds



**Figure 2.12:** The distribution of energy loss as a function of reconstructed momentum for charged particles passing through the TPC, comparing data to Monte Carlo prediction. Taken from [114].

hindering the electron neutrino appearance searches. Therefore, the  $\pi^0$  detector (P0D) measures the cross-section of the neutral current induced neutral pion production on a water target.

The P0D is a cube of approximately 2.5m length. The P0D consists of layers of scintillating bars, brass and lead sheets, and water bags as illustrated in Figure 2.13. Two electromagnetic calorimeters are positioned at the most upstream and most downstream position in the sub-detector and the water target is situated in between them. The scintillator layers are built from two triangular bars orientated in opposite directions to form a rectangular layer. Each triangular scintillator bar is threaded with optical fiber which is read out by MPPCs. The high-Z brass and lead regions produce electron showers from the photons emitted in  $\pi^0$  decay.

The sub-detector can generate measurements of NC1 $\pi^0$  cross-sections on a water target by measuring the event rate both with and without the water target, with the cross-section on a water target being determined as the difference. The total active mass is 16.1 tonnes when filled with water and 13.3 tonnes when empty.

#### 2.2.2.4 Electromagnetic Calorimeter

The electromagnetic calorimeter [116] (ECal) encapsulates the P0D and tracking sub-detectors. Its primary purpose is to aid  $\pi^0$  reconstruction from any interaction in the tracker. To do this, it measures the energy and direction of photon showers from  $\pi^0 \rightarrow 2\gamma$  decay. It can also distinguish pion and muon tracks depending on the shape of the photon shower deposited.

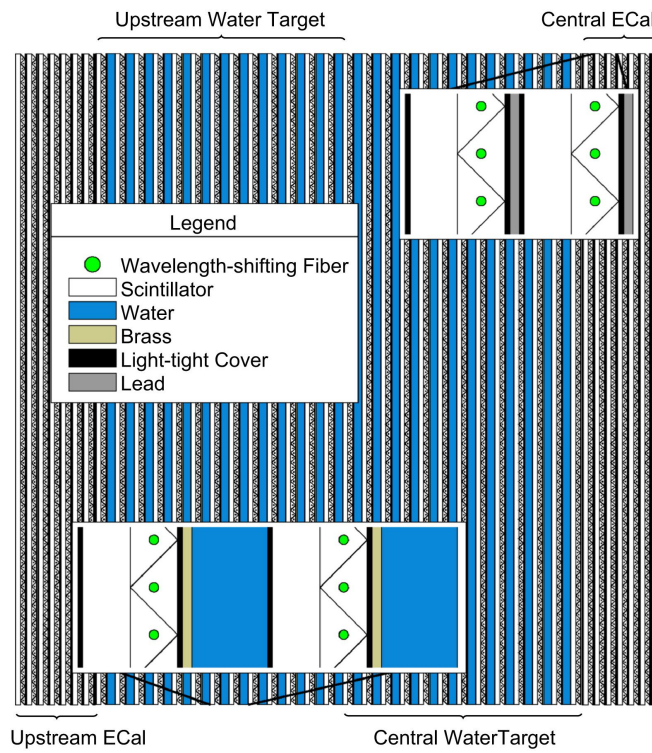


**Figure 2.13:** A schematic of the P0D side-view. Taken from [115].

825     The ECal is comprised of three sections; the P0D ECal which surrounds the P0D,  
 826     the barrel ECal which encompasses the tracking region, and the downstream ECal  
 827     which is situated downstream of the tracker region. The barrel and downstream  
 828     ECals are tracking calorimeters that focus on electromagnetic showers from high-angle  
 829     particles emitted from the tracking sub-detectors. Particularly in the TPC, high-angle  
 830     tracks (those which travel perpendicularly to the beam-axis) can travel along a single  
 831     scintillator bar resulting in very few hits. The width of the barrel and downstream  
 832     ECal corresponds to  $\sim 11$  electron radiation lengths to ensure  $\sim 50\%$  of the energy of  
 833     the  $\pi^0$  is contained. As the P0D has its own calorimetry which reconstructs showers,  
 834     the P0D ECal determines the energy which escapes the P0D.

835     Each ECal is constructed of multiple layers of scintillating bars sandwiched between  
 836     lead sheets. The scintillating bars are threaded with optical fiber and read out by  
 837     MPPCs. Each sequential layer of the scintillator is orientated perpendicular to the  
 838     previous which allows a two-dimensional readout, which when temporal information  
 839     is included results in three-dimension event displays. The target mass of the P0D ECal,  
 840     barrel ECal, and downstream ECal are 1.50, 4.80 and 6.62 tonnes respectively.

**841 2.2.2.5 Side Muon Range Detector**

842 As illustrated in Figure 2.9, the ECal, FGDs, P0D, and TPCs are enclosed within the  
 843 UA1 magnet. Originally designed for the NOMAD [117] experiment and reconditioned  
 844 for use in the T2K experiment [118], the UA1 magnet provides a uniform horizontal  
 845 magnetic field of  $0.2 \pm 2 \times 10^{-4}$ T.

846 Built into the UA1 magnet, the side muon range detector (SMRD) [119] monitors  
 847 high-energy muons which leave the tracking region and permeate through the ECal.  
 848 It additionally acts as a cosmic muon veto and trigger.

**849 2.2.3 The Interactive Neutrino GRID**

850 The Interactive Neutrino GRID (INGRID) detector is situated within the same “pit” as  
 851 the other near detectors. It is aligned with the beam in the “on-axis” position and mea-  
 852 sures the beam direction, spread, and intensity. The detector was originally designed  
 853 with 16 identical modules [108] (two modules have since been decommissioned) and a  
 854 “proton” module. The design of the detector is cross-shaped with length and height  
 855 10m × 10m as illustrated in Figure 2.14.

856 Each module is composed of iron sheets interlaced with eleven tracking scintillator  
 857 planes for a total target mass of 7.1 tonnes per module. The scintillator design is an X-Y  
 858 pattern of 24 bars in both orientations, where each bar contains wave-length shifting  
 859 fibers which are connected to multi-pixel photon counters (MPPCs). The MPPCs  
 860 convert detected photons into electrical signals via photodiodes. This is then read  
 861 out by Trip-T front-end electronics [120] and passed to the readout merging modules  
 862 along with timing information from the clock module. Each module is encapsulated  
 863 inside veto planes to aid the rejection of charged particles entering the module.

864 The proton module is different from the other modules in that it consists of entirely  
 865 scintillator planes with no iron target. The scintillator bars are also smaller than those  
 866 used in the other modules to increase the granularity of the detector and improve  
 867 tracking capabilities. The module sits in the center of the beamline and is designed to  
 868 give precise measurements of quasi-elastic charged current interactions to evaluate  
 869 the performance of the Monte Carlo simulation of the beamline.

870 The INGRID detector can measure the beam direction to an uncertainty of 0.4mrad  
 871 and the beam center within a resolution of 10cm [108]. The beam direction in both the

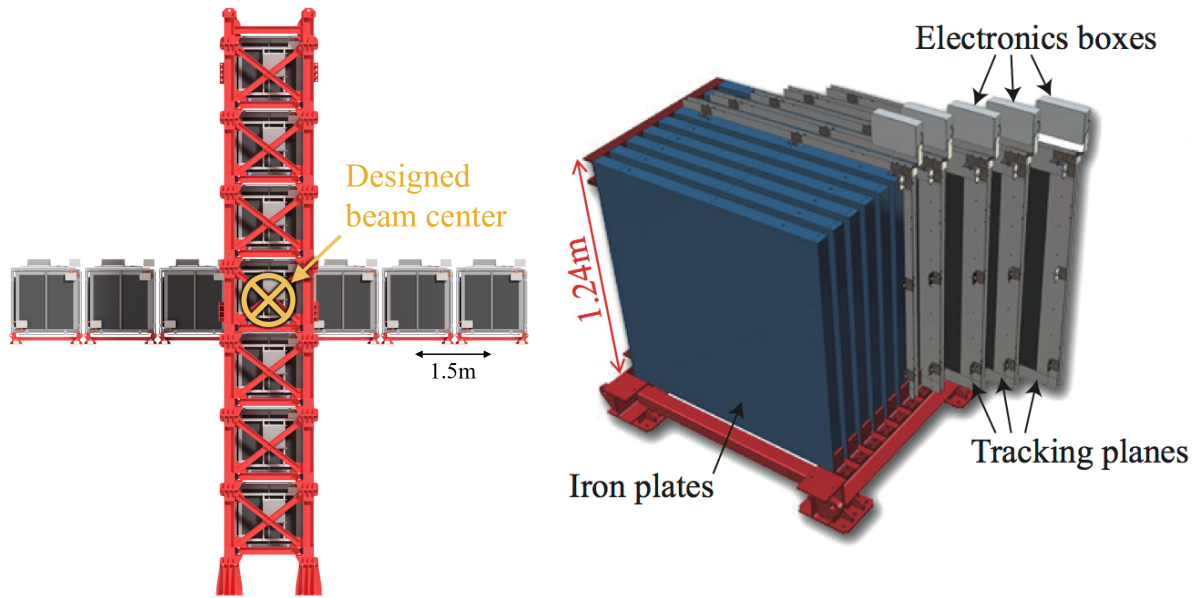


**Figure 2.14:** Left panel: The Interactive Neutrino GRID on-axis Detector. 14 modules are arranged in a cross-shape configuration, with the center modules being directly aligned with the on-axis beam. Right panel: The layout of a single module of the INGRID detector. Both figures are recreated from [108].

<sup>872</sup> vertical and horizontal directions is discussed in [121] and it is found to be in good  
<sup>873</sup> agreement with the MUMON monitor described in subsection 2.2.1.

874 **Chapter 3**

875 **Bayesian Statistics Implemented Through**  
876 **Markov Chain Monte Carlo Techniques**

877 The analysis throughout this thesis is based upon a Bayesian oscillation analysis. To  
878 extract the oscillation parameters, a Markov Chain Monte Carlo (MCMC) method is  
879 used. This chapter explains the theory of how parameter estimates can be determined  
880 using this technique and condenses the material found in the literature [122–125].

881 The oscillation parameter determination presented within this thesis is built upon a  
882 simultaneous fit to the near detector, far detector beam, and atmospheric neutrino data.  
883 In total, there are four oscillation parameters of interest ( $\sin^2(\theta_{23})$ ,  $\sin^2(\theta_{13})$ ,  $\Delta m_{23}^2$ , and  
884  $\delta_{CP}$ ), two oscillation parameters to which this study will not be sensitive ( $\sin^2(\theta_{12})$ ,  
885  $\Delta m_{12}^2$ ) and many nuisance parameters that control the systematic uncertainty models  
886 invoked within this study. The systematic uncertainties can be grouped into categories  
887 depending on how they are defined; 574 bin-normalisations due to the near detector  
888 response, 45 bin-normalisations to describe the far detector response to neutrino beam  
889 events, 27 parameters to describe the detector response to atmospheric neutrino events,  
890 100 to model the bin-normalisation due to beam flux uncertainties, 18 which model the  
891 atmospheric flux uncertainties, and 87 to describe the correlated cross-section model.  
892 An alternative parameterisation, where the far detector response is correlated between  
893 the beam and atmospheric samples, replaces the bin-normalisation parameters with  
894 224 shift and smear systematics. Section [DB: Link to Systematics Chapter](#) describes  
895 the systematic model in more depth.

896 The MCMC technique generates a multi-dimensional probability distribution across  
897 all of the model parameters used in the fit. To determine the parameter estimate of a  
898 single parameter, this multi-dimensional object is integrated over all other parameters.  
899 This process is called Marginalisation and is further described in subsection 3.3.1.  
900 Monte Carlo techniques approximate the probability distribution of each parameter  
901 within the limit of generating infinite samples. As ever, generating a large number of  
902 samples is time and resource-dependent. Therefore, an MCMC technique is utilised

within this analysis to reduce the required number of steps to sufficiently sample the parameter space. This technique is described in further detail in subsection 3.2.1.

### 3.1 Bayesian Statistics

According to Bayesian Inference, observables and parameters of a statistical model are treated on an equal footing. To estimate model parameters  $\vec{\theta}$  from some data  $D$ , one needs to define the joint probability distribution  $P(D|\vec{\theta})$  which can be described as the prior distribution for model parameters  $P(\vec{\theta})$  and the likelihood of the data given the model parameters  $P(D|\vec{\theta})$ ,

$$P(D, \vec{\theta}) = P(D|\vec{\theta})P(\vec{\theta}). \quad (3.1)$$

The prior distribution,  $P(\vec{\theta})$ , describes all previous knowledge about the parameters within the model. For example, if the risk of developing health problems is known to increase with age, the prior distribution would describe the increase. For the purpose of this analysis, the prior distribution is typically the best-fit values taken from external data measurements with a Gaussian uncertainty. The prior distribution can also contain correlations between model parameters. In an analysis using Monte Carlo techniques, the likelihood of measuring some data assuming some set of model parameters is calculated by comparing the Monte Carlo prediction generated at that particular set of model parameters to the data.

It is parameter estimation that is important for this analysis and as such, we apply Bayes' theorem [126]. To calculate the probability for each parameter to have a certain value given the observed data  $P(\vec{\theta}|D)$ , known as the posterior distribution (often termed the posterior). This can be expressed as

$$P(\vec{\theta}|D) = \frac{P(D|\vec{\theta})P(\vec{\theta})}{\int P(D|\vec{\theta})P(\vec{\theta})d\vec{\theta}}. \quad (3.2)$$

## **Bayesian Statistics Implemented Through Markov Chain Monte Carlo Techniques**

924        The denominator in Equation 3.2 is the integral of the joint probability distribution  
925   over all values of all parameters used within the fit. For brevity, we say that the  
926   posterior distribution is

$$P(\vec{\theta}|D)\alpha P(D|\vec{\theta})P(\vec{\theta}). \quad (3.3)$$

927        In subsection 3.3.1, we see that for the cases used within this analysis, it is reason-  
928   able to know the posterior to some normalisation constant.

## **3.2 Monte Carlo Simulation**

930        Monte Carlo techniques are used to numerically solve a complex problem that does  
931   not necessarily have an analytical solution. These techniques rely on building a large  
932   ensemble of samples from an unknown distribution and then using the ensemble to  
933   approximate the properties of the distribution.

934        An example that uses Monte Carlo techniques is to calculate the area underneath  
935   a curve. For example, take the problem of calculating the area under a straight line  
936   with gradient  $M = 0.4$  and intercept  $C = 1.0$ . Analytically, one can calculate the area  
937   under the line is equal to 30 units for  $0 \leq x \leq 10$ . Using Monte Carlo techniques,  
938   one can calculate the area under this line by throwing many random values for the  $x$   
939   and  $y$  components of each sample and then calculating whether that point falls below  
940   the line. The area can then be calculated by the ratio of points below the line to the  
941   total number of samples thrown multiplied by the total area in which samples were  
942   scattered. The study is shown in Figure 3.1 highlights this technique and finds the area  
943   under the curve to be 29.9 compared to an analytical solution of 30.0. The deviation  
944   of the numerical to analytical solution can be attributed to the number of samples  
945   used in the study. The accuracy of the approximation in which the properties of the  
946   Monte Carlo samples replicate those of the desired distribution is dependent on the  
947   number of samples used. Replicating this study with a differing number of Monte  
948   Carlo samples used in each study (As shown in Figure 3.2) highlights how the Monte  
949   Carlo techniques are only accurate within the limit of a high number of samples.

Whilst the above example has an analytical solution, these techniques are just as applicable to complex solutions. Clearly, any numerical solution is only as useful as its efficiency. As discussed, the accuracy of the Monte Carlo technique is dependent upon the number of samples generated to approximate the properties of the distribution. Furthermore, if the positions at which the samples are evaluated are not ‘cleverly’ picked, the efficiency of the Monte Carlo technique significantly drops. Given the example in Figure 3.1, if the region in which the samples are scattered significantly extends passed the region of interest, many calculations will be calculated but do not add to the ability of the Monte Carlo technique to achieve the correct result. For instance, any sample evaluated at a  $y \geq 5$  could be removed without affecting the final result. This does bring in an aspect of the ‘chicken and egg’ problem in that to achieve efficient sampling, one needs to know the distribution beforehand.

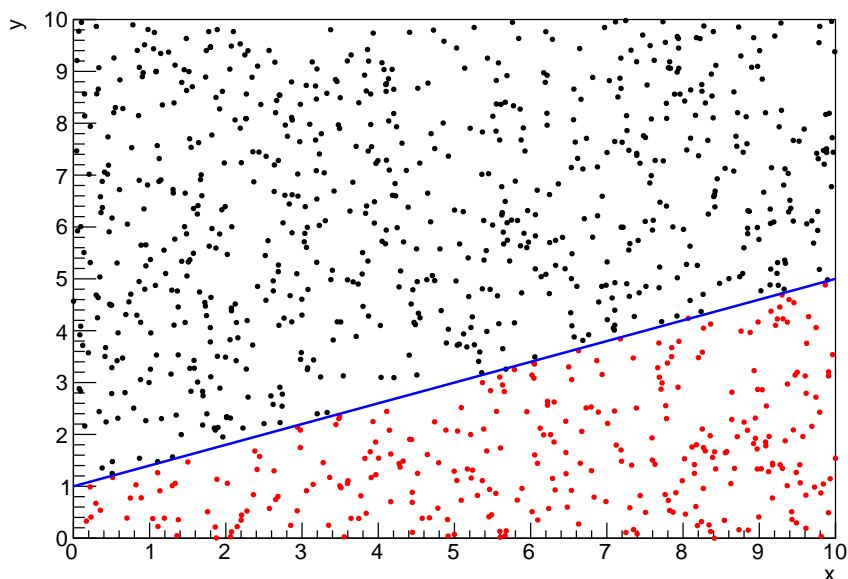


**Figure 3.1:** Example of using Monte Carlo techniques to find the area under the blue line. The gradient and intercept of the line are 0.4 and 1.0 respectively. The area found to be under the curve using one thousand samples is 29.9 units.

### 3.2.1 Markov Chain Monte Carlo

This analysis utilises a multi-dimensional probability distribution, with some dimensions being significantly more constrained than others. This could be from prior knowledge of parameter distributions from external data or un-physical regions in

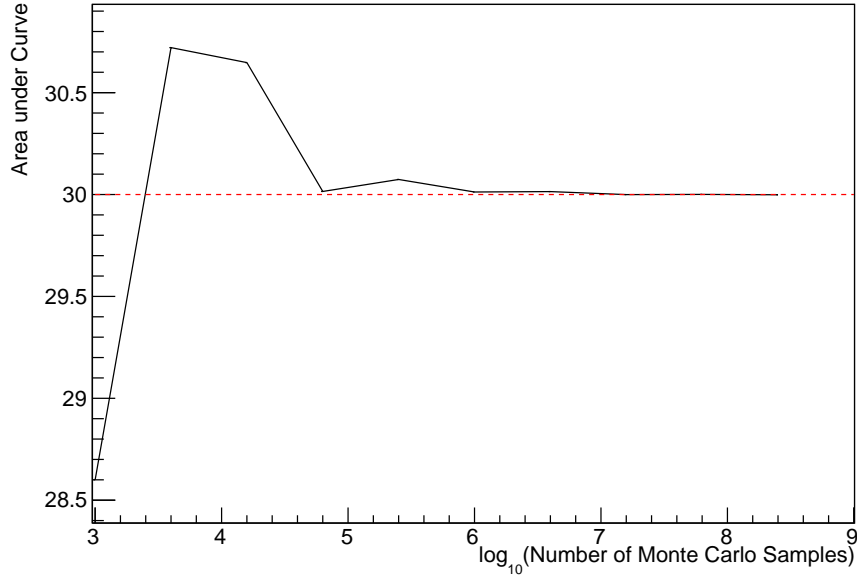


**Figure 3.2:** The area under a line of gradient 0.4 and intercept 1.0 for the range  $0 \leq x \leq 10$  as calculated using Monte Carlo techniques as a function of the number of samples used in each repetition. The analytical solution to the area is 30 units as given by the red line.

which parameters can not exist. Consequently, the Monte Carlo techniques used need to be as efficient as possible. For this analysis, the Markov Chain Monte Carlo (MCMC) technique is chosen. An MCMC technique is a Monte Carlo technique that uses a Markov chain to select which points at which to sample the parameter distribution. This technique performs a semi-random stochastic walk through the allowable parameter space. This builds a posterior distribution which has the property that the density of sampled points is proportional to the probability density of that parameter. This does mean that the samples produced by this technique are not statistically independent but they will cover the space of the distribution.

A Markov chain functions by selecting the position of step  $\vec{x}_{i+1}$  based on the position of  $\vec{x}_i$ . The space in which the Markov chain selects samples is dependent upon the total number of parameters utilised within the fit, where a discrete point in this space is described by the N-dimensional space  $\vec{x}$ . In a perfectly operating Markov chain, the position of the next step depends solely on the previous step and not on the further history of the chain ( $\vec{x}_0, \vec{x}_1$ , etc.). However, in solving the multi-dimensionality of the fit used within this analysis, each step becomes correlated with several of the steps preceding itself. This behaviour is further explained in subsection 3.2.3. Providing the MCMC chain is well optimised, it will begin to converge towards a

unique stationary distribution. The period between the chain's initial starting point and the convergence to the unique stationary distribution is colloquially known as the burn-in period. This is discussed further in subsection 3.2.3. Once the chain reaches the stationary distribution, all points sampled after that point will look like samples from that distribution.

Further details of the theories underpinning MCMC techniques are discussed in [123] but can be summarised by the requirement that the chain satisfies the three 'regularity conditions':

- Irreducibility: From every position in the parameter space  $\vec{x}$ , there must exist a non-zero probability for every other position in the parameter space to be reached.
- Recurrence: Once the chain arrives at the stationary distribution, every step following from that position must be samples from the same stationary distribution.
- Aperiodicity: The chain must not repeat the same sequence of steps at any point throughout the sampling period.

The output of the chain after burn-in (ie. the sampled points after the chain has reached the stationary distribution) can be used to approximate the posterior distribution and model parameters  $\vec{\theta}$ . To achieve the requirement that the unique stationary distribution found by the chain be the posterior distribution, one can use the Metropolis-Hastings algorithm. This guides the stochastic process depending on the likelihood of the current proposed step compared to that of the previous step. Implementation and other details of this technique are discussed in subsection 3.2.2.

### 3.2.2 Metropolis-Hastings Algorithm

As a requirement for MCMCs, the Markov chain implemented in this technique must have a unique stationary distribution that is equivalent to the posterior distribution. To ensure this requirement and that the regularity conditions are met, this analysis utilises the Metropolis-Hastings (MH) algorithm [127,128]. For the  $i^{th}$  step in the chain, the MH algorithm determines the position in the parameter space to which the chain moves to based on the current step,  $\vec{x}_i$ , and the proposed step,  $\vec{y}_{i+1}$ . The proposed step is randomly selected from some proposal function  $f(\vec{x}_{i+1}|\vec{x}_i)$ , which depends solely on the current step (ie. not the further history of the chain). The next step in the chain  $\vec{x}_{i+1}$  can be either the current step or the proposed step determined by whether the

## Bayesian Statistics Implemented Through Markov Chain Monte Carlo Techniques

1015 proposed step is accepted or rejected. To decide if the proposed step is selected, the  
1016 acceptance probability,  $\alpha(\vec{x}_i, \vec{y}_i)$ , is calculated as

$$\alpha(\vec{x}_i, \vec{y}_{i+1}) = \min \left( 1, \frac{P(\vec{y}_{i+1}|D)f(\vec{x}_i|\vec{y}_{i+1})}{P(\vec{x}_i|D)f(\vec{y}_{i+1}|\vec{x}_i)} \right). \quad (3.4)$$

1017 Where  $P(\vec{y}_{i+1}|D)$  is the posterior distribution as introduced in section 3.1. To  
1018 simplify this calculation, the proposal function is required to be symmetric such that  
1019  $f(\vec{x}_i|\vec{y}_{i+1}) = f(\vec{y}_{i+1}|\vec{x}_i)$ . In practice, a multi-variate Gaussian distribution is used to  
1020 throw parameter proposals from. This reduces Equation 3.4 to

$$\alpha(\vec{x}_i, \vec{y}_{i+1}) = \min \left( 1, \frac{P(\vec{y}_{i+1}|D)}{P(\vec{x}_i|D)} \right). \quad (3.5)$$

1021 After calculating this quantity, a random number,  $\beta$ , is generated uniformly be-  
1022 tween 0 and 1. If  $\beta \leq \alpha(\vec{x}_i, \vec{y}_{i+1})$ , the proposed step is accepted. Otherwise, the chain  
1023 sets the next step equal to the current step and this procedure is repeated. This can be  
1024 interpreted as if the posterior probability of the proposed step is greater than that of  
1025 the current step, ( $P(\vec{y}_{i+1}|D) \geq P(\vec{x}_i|D)$ ), the proposed step will always be accepted.  
1026 If the opposite is true, ( $P(\vec{y}_{i+1}|D) \leq P(\vec{x}_i|D)$ ), the proposed step will be accepted  
1027 with probability  $P(\vec{x}_i|D)/P(\vec{y}_{i+1}|D)$ . This ensures that the Markov chain does not get  
1028 trapped in any local minima in the potentially non-Gaussian posterior distribution.  
1029 The outcome of this technique is that the density of steps taken in a discrete region is  
1030 directly proportional to the probability density in that region.

### 1031 3.2.3 MCMC Optimisation

1032 As discussed in subsection 3.2.2, the proposal function invoked within the MH algo-  
1033 rithm can take any form and the chain will still converge to the stationary distribution.  
1034 As discussed in [DB: Link to Analysis Strategy Section](#), this analysis performs the  
1035 Monte Carlo reweighting on an event-by-event basis. This requires significant com-  
1036 putational resources to perform a parameter fit. Therefore, the number of steps taken  
1037 before the unique stationary distribution is found should be minimised as only steps  
1038 after convergence add information to the fit. Furthermore, the chain should entirely

1039 cover the allowable parameter space to ensure that all values have been considered.  
1040 Tuning the distance that the proposal function jumps between steps on a parameter-  
1041 by-parameter basis can both minimise the length of the burn-in period and ensure that  
1042 the correlation between step  $\vec{x}_i$  and  $\vec{x}_j$  is sufficiently small.

1043 The effect of changing the width of the proposal function is highlighted in Figure 3.3.  
1044 Three scenarios, each with the same underlying stationary distribution (A Gaussian of  
1045 width 1.0 and mean 0.), are presented. The only difference between the three scenarios  
1046 is the width of the proposal function, colloquially known as the ‘step size  $\sigma$ ’. Each  
1047 scenario starts at an initial parameter value of 10.0 which would be considered an  
1048 extreme variation. For the case where  $\sigma = 0.1$ , it is clear to see that the chain takes  
1049 a long time to reach the expected region of the parameter. This indicates that this  
1050 chain would have a large burn-in period and does not converge to the stationary  
1051 distribution until step  $\sim 500$ . Furthermore, whilst the chain does move towards the  
1052 expected region, each step is significantly correlated with the previous. Considering  
1053 the case where  $\sigma = 5.0$ , the chain approaches the expected parameter region almost  
1054 instantly meaning that the burn-in period is not significant. However, there are clearly  
1055 large regions of steps where the chain does not move. This is likely due to the chain  
1056 proposing steps in the tails of the distribution which have a low probability of being  
1057 accepted. Consequently, this chain would take a significant number of steps to fully  
1058 span the allowable parameter region. For the final scenario, where  $\sigma = 0.5$ , you can see  
1059 a relatively small burn-in period of approximately 100 steps. Once the chain reaches  
1060 the stationary distribution, it moves throughout the expected region of parameter  
1061 values many times, sufficiently sampling the full parameter region. This example is a  
1062 single parameter varying across a continuous distribution and does not fully reflect  
1063 the difficulties in the many-hundred multi-variate parameter distribution used within  
1064 this analysis. However, it does give a conceptual idea of the importance of selecting  
1065 the proposal function and associated step size.

1066 As discussed, step size tuning directly correlates to the average step acceptance  
1067 rate. If the step size is too small, many steps will be accepted but the chain moves  
1068 slowly. If the opposite is true, many steps will be rejected as the chain proposes steps  
1069 in the tails of the distribution. Discussion in [129] suggests that the ‘ideal’ acceptance  
1070 rate of a high dimension MCMC chain should be approximately  $\sim 25\%$ . An “ideal”  
1071 step size [129] of

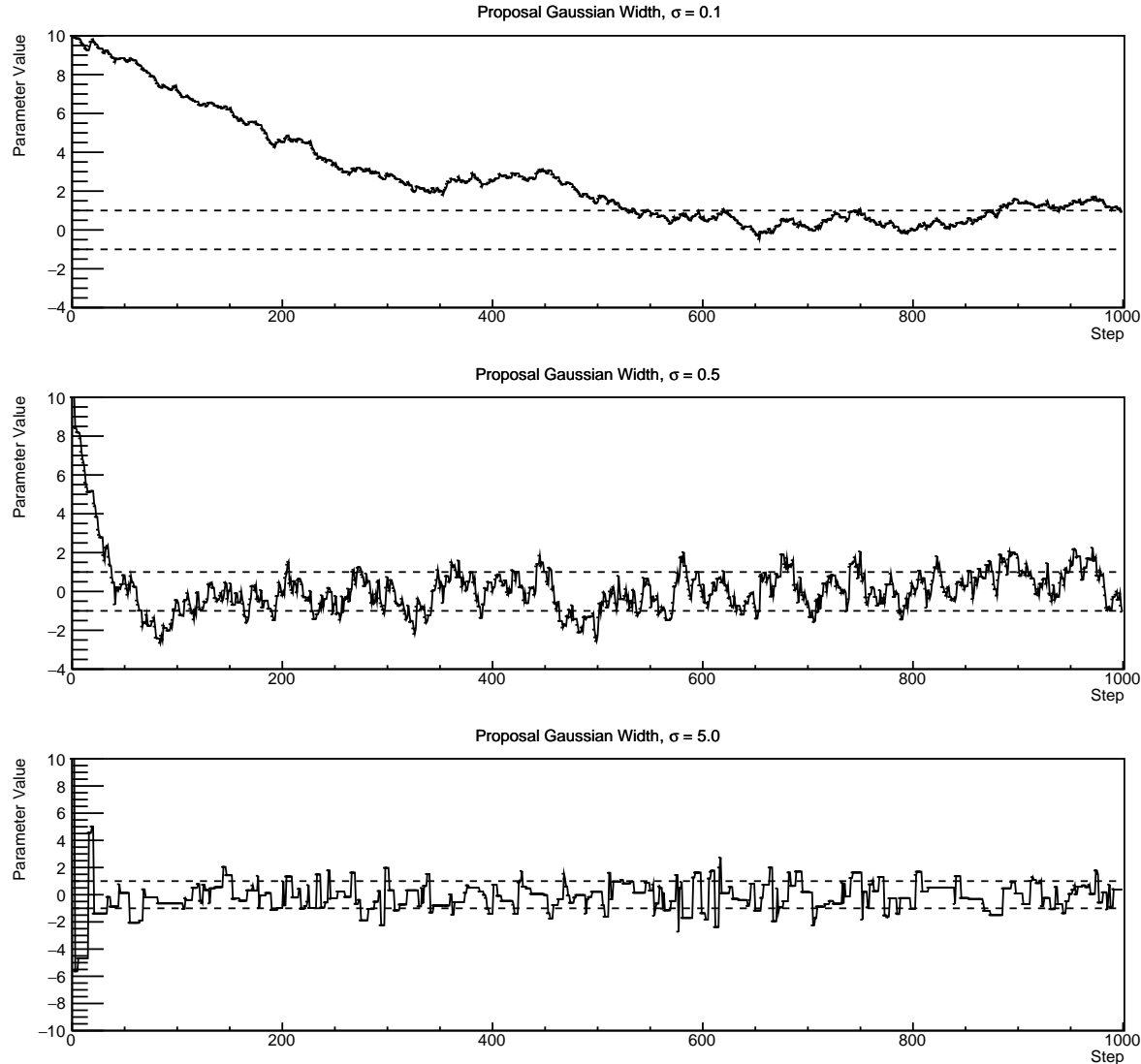


**Figure 3.3:** Three MCMC chains, each with a stationary distribution equal to a Gaussian centered at 0 and width 1 (As indicated by the black dotted lines). All of the chains use a Gaussian proposal function but have different widths (or ‘step size  $\sigma$ ’). The top panel has  $\sigma = 0.1$ , middle panel has  $\sigma = 0.5$  and the bottom panel has  $\sigma = 5.0$ .

$$\sigma = \frac{2.4}{N_p}, \quad (3.6)$$

where  $N_p$  is the number of parameters included in the MCMC fit. However, the complex correlations between systematics mean that some parameters have to be hand tuned and many efforts have been taken to select a set of parameter-by-parameter step sizes to approximately reach the ideal acceptance rate.

1076     Figure 3.3 highlights the likelihood as calculated by the fit in DB: Link to AsimovA  
 1077     Sensitivity Section as a function of the number of steps in each chain. In practice,  
 1078     many independent MCMC chains are run simultaneously to parallelise the task of  
 1079     performing the fit. This figure overlays the distribution found in each chain. As seen,  
 1080     the likelihood decreases from its initial value and converges towards a stationary  
 1081     distribution after  $\sim 1 \times 10^5$  steps. Each fit (whether it be different asimov fits or data  
 1082     fit) will have a different set of preferred parameter values which results in a different  
 1083     stationary distribution. For each fit presented in this thesis, a burn-in period of  $1 \times 10^5$   
 1084     steps was found to be sufficient.

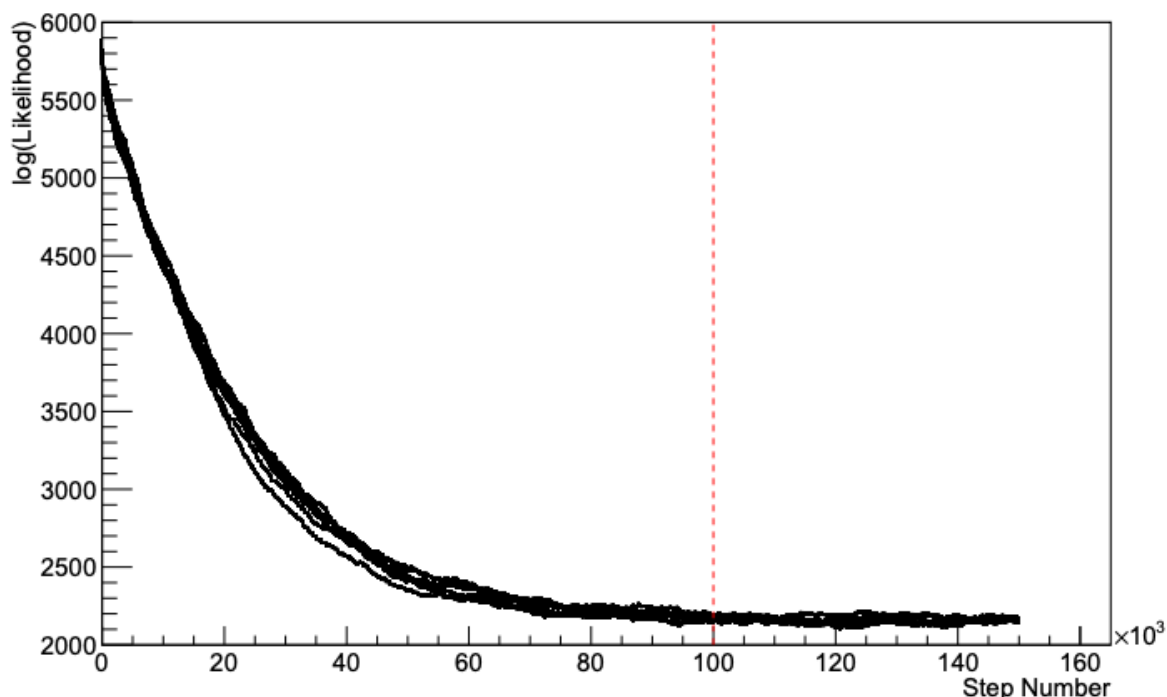


Figure 3.4: The log-likelihood from the fit detailed in DB: Link to AsimovA Sensitivity Section as a function of the number of steps accumulated in each fit. Many independent MCMC chains were run in parallel and overlaid on this plot. The red line indicates the  $1 \times 10^5$  step burn-in period after which the log-likelihood becomes stable.

### 1085 3.3 Understanding the MCMC Results

1086 Whilst section 3.1 and section 3.2 describe how to interpret Bayesian statistics and  
 1087 explains the MCMC techniques used within this analysis, there is no mention of  
 1088 how to interpret the output of the chain. The posterior distribution output from the

chain is a high dimension object, with as many dimensions as there are parameters included in the fit. However, this multi-dimensional object is difficult to conceptualize so parameter estimations are often presented in one or two-dimensional projections of this probability distribution. To do this, we invoke the marginalisation technique highlighted in subsection 3.3.1.

### **3.3.1 Marginalisation**

The output of the MCMC chain is a highly dimensional probability distribution which is very difficult to interpret. From the standpoint of an oscillation analysis experiment, the one or two-dimensional ‘projections’ of the oscillation parameters of interest are most relevant. Despite this, the best fit values and uncertainties on the oscillation parameters of interest should correctly encapsulate the correlations to the other systematic uncertainties (colloquially called ‘nuisance’ parameters). For this joint beam and atmospheric analysis, the oscillation parameters of interest are  $\sin^2(\theta_{23})$ ,  $\sin^2(\theta_{13})$ ,  $\Delta m_{23}^2$ , and  $\delta_{CP}$ . All other parameters (Including the oscillation parameter this fit is insensitive to) are deemed nuisance parameters. To generate these projections, we rely upon integrating the posterior distribution over all nuisance parameters. This is called marginalisation. A simple example of this technique is to imagine the scenario where two coins are flipped. To determine the probability that the first coin returned a ‘head’, the exact result of the second coin flip is disregarded and simply integrated over. For the parameters of interest,  $\vec{\theta}_i$ , we can calculate the marginalised posterior by integrating over the nuisance parameters,  $\vec{\theta}_n$ . In this case, Equation 3.2 becomes

$$P(\vec{\theta}_i|D) = \frac{\int P(D|\vec{\theta}_i, \vec{\theta}_n)P(\vec{\theta}_i, \vec{\theta}_n)d\vec{\theta}_n}{\int P(D|\vec{\theta})P(\vec{\theta})d\vec{\theta}} \quad (3.7)$$

Where  $P(\vec{\theta}_i, \vec{\theta}_n)$  encodes the prior knowledge about the uncertainty and correlations between the parameters of interest and the nuisance parameters. In practice, this is simply taking the one or two-dimensional projection of the multi-dimensional probability distribution.

Whilst in principle an easy solution to a complex problem, correlations between the interesting and nuisance parameters can bias the marginalised results. A similar effect is found when the parameters being marginalised over have non-Gaussian probability

distributions. For example, Figure 3.5 highlights the marginalisation bias in the probability distribution found for a parameter when requiring a correlated parameter to have a positive parameter value. Due to the complex nature of this oscillation parameter fit presented in this thesis, there are certainly correlations occurring between the oscillation parameters of interest and the other nuisance parameters included in the fit.

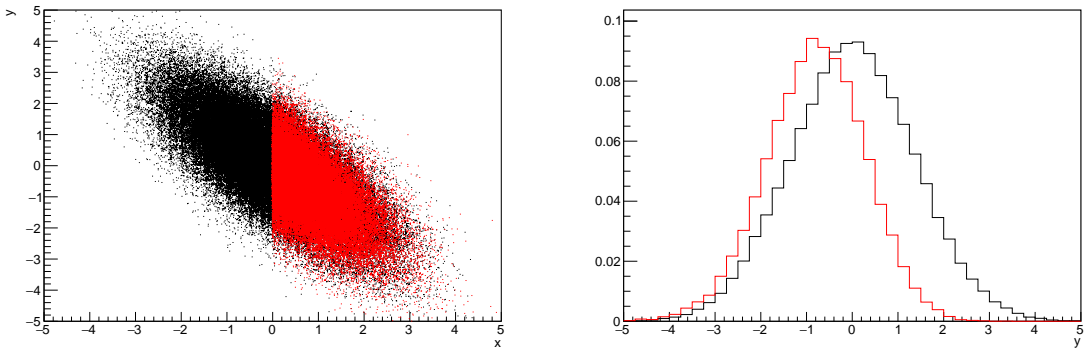


**Figure 3.5:** Left: The two dimensional probability distribution for two correlated parameters  $x$  and  $y$ . The red distribution shows the two dimensional probability distribution when  $0 \leq x \leq 5$ . Right: The marginalised probability distribution for the  $y$  parameter found when requiring the  $x$  to be bound between  $-5 \leq x \leq 5$  and  $0 \leq x \leq 5$  for the black and red distribution, respectively.

### 3.3.2 Parameter Estimation and Credible Intervals

The purpose of this analysis is to determine the best fit values for the oscillation parameters that the beam and atmospheric samples are sensitive to;  $\sin^2(\theta_{23})$ ,  $\sin^2(\theta_{13})$ ,  $\Delta m_{23}^2$ , and  $\delta_{CP}$ . Typically, the results presented take the form of one or two-dimension marginalised probability distributions for the appearance ( $\sin^2(\theta_{13})$  and  $\delta_{CP}$ ) and disappearance ( $\sin^2(\theta_{23})$  and  $\Delta m_{23}^2$ ) parameters. The posterior probability density taken from the output MCMC chain is binned in these parameters. The parameter best-fit point is then taken to be the value that has the highest posterior probability. This is performed in both one and two-dimensional projections.

However, the single best-fit point in a given parameter is not of much use on its own. We would also like to determine the uncertainty, or credible interval, on that best-fit point. The definition of the  $1\sigma$  credible interval is that we have 68% belief that the parameter is within those bounds. For a more generalised definition, the credible

## Bayesian Statistics Implemented Through Markov Chain Monte Carlo Techniques

<sub>1136</sub> interval is the region of the posterior distribution that contains a specific fraction of  
<sub>1137</sub> the total probability, such that

$$\int P(\theta|D)d\theta = \alpha \quad (3.8)$$

<sub>1138</sub> Where  $\theta$  is the parameter on which we calculate the credible interval. This technique  
<sub>1139</sub> then calculates the  $\alpha \times 100\%$  credible interval.

<sub>1140</sub> In practice, this analysis uses the highest posterior density (HPD) credible intervals  
<sub>1141</sub> which are calculated through the following method. First, the probability distribution  
<sub>1142</sub> is area-normalised such that it has an integrated area equal to 1.0. The bins of proba-  
<sub>1143</sub> bility are then summed from the highest to lowest until the sum exceeds the  $1\sigma$  level  
<sub>1144</sub> (0.68 in this example). This process is repeated for a range of credible intervals, notably  
<sub>1145</sub> the  $1\sigma$ ,  $2\sigma$  and  $3\sigma$  along with other levels where the critical values for each level can  
<sub>1146</sub> be found in [130]. This process can be repeated for the two-dimensional probability  
<sub>1147</sub> distributions by creating two-dimensional contours of credible intervals rather than a  
<sub>1148</sub> one-dimensional result.

### <sub>1149</sub> 3.3.3 Application of Bayes' Theorem

<sub>1150</sub> Due to the matter resonance, this analysis has some sensitivity to the mass hierarchy of  
<sub>1151</sub> neutrino states (whether  $\Delta m_{23}^2$  is positive or negative) and the octant of  $\sin^2(\theta_{23})$ . The  
<sub>1152</sub> Bayesian approach utilised within this analysis gives an intuitive method of model  
<sub>1153</sub> comparison by determining which hypothesis is most favourable. Taking the ratio of  
<sub>1154</sub> Equation 3.3 for the two hypotheses of normal hierarchy,  $NH$ , and inverted hierarchy,  
<sub>1155</sub>  $IH$ , gives

$$\frac{P(\vec{\theta}_{NH}|D)}{P(\vec{\theta}_{IH}|D)} = \frac{P(D|\vec{\theta}_{NH})}{P(D|\vec{\theta}_{IH})} \times \frac{P(\vec{\theta}_{NH})}{P(\vec{\theta}_{IH})}. \quad (3.9)$$

<sub>1156</sub> The middle term defines the Bayes factor which is a data-driven interpretation of  
<sub>1157</sub> how strong the data prefers one hierarchy to the other. For this analysis, equal priors  
<sub>1158</sub> on both mass hierarchy hypotheses are chosen ( $P(\vec{\theta}_{NH}) = P(\vec{\theta}_{IH}) = 0.5$ ). In practice,

1159 the MCMC chain proposes a value of  $|\Delta m_{23}^2|$  and then applies a 50% probability that  
 1160 the value is sign flipped. Consequently, the Bayes factor can be calculated from the  
 1161 ratio of the probability density in either hypothesis. This equates to counting the  
 1162 number of steps taken in the normal and inverted hierarchies and taking the ratio. The  
 1163 same approach can be taken to compare the upper octant (UO) compared to the lower  
 1164 octant (LO) hypothesis of  $\sin^2(\theta_{23})$ .

1165 Whilst the value of the Bayes factor should always be shown, the Jeffreys scale [131]  
 1166 (highlighted in Table 3.1) gives an indication of the strength of preference for one model  
 1167 compared to the other. Other interpretations of the strength of preference of a model  
 1168 exist, e.g. the Kass and Raferty Scale [132].

$\log_{10}(B_{AB})$	$B_{AB}$	Strength of Preference
< 0.0	< 1	No preference for hypothesis A (Supports hypothesis B)
0.0 – 0.5	1.0 – 3.16	Preference for hypothesis A is weak
0.5 – 1.0	3.16 – 10.0	Preference for hypothesis A is substantial
1.0 – 1.5	10.0 – 31.6	Preference for hypothesis A is strong
1.5 – 2.0	31.6 – 100.0	Preference for hypothesis A is very strong
> 2.0	> 100.0	Decisive preference for hypothesis A

**Table 3.1:** Jeffreys scale for strength of preference for two models  $A$  and  $B$  as a function of the calculated Bayes factor ( $B_{AB} = B(A/B)$ ) between the two models [131]. The original scale is given in terms of  $\log_{10}(B(A/B))$  but converted to linear scale for easy comparison throughout this thesis.

### 1169 3.3.4 Comparison of MCMC Output to Expectation

1170 Whilst not important for the extraction of oscillation parameters, understanding how  
 1171 the data constrains the model parameters is important to the understanding of this  
 1172 analysis. A simple method of doing this is to perform a comparison in the fitting  
 1173 parameters (For instance, the reconstructed neutrino energy and lepton direction for  
 1174 T2K far detector beam samples) of the spectra generated by the MCMC chain to ‘data’.  
 1175 This ‘data’ could be true data or some variation of Monte Carlo prediction. This allows  
 1176 easy comparison of the MCMC probability distribution to the data. To perform this,  $N$   
 1177 steps from the post burn-in MCMC chain are randomly selected (Where for all plots  
 1178 of this style in this thesis,  $N = 3000$ ). From these, the Monte Carlo prediction at each  
 1179 step is generated by reweighting the model parameters to the values specified at that

## Bayesian Statistics Implemented Through Markov Chain Monte Carlo Techniques

1180 step. Due to the probability density being directly correlated with the density of steps  
1181 in a certain region, parameter values close to the best fit value are most likely to be  
1182 selected.

1183 In practice, for each bin of the fitting parameters has a probability distribution  
1184 of event rates, with one entry per sampled MCMC step. This distribution is binned  
1185 where the bin with the highest probability is selected as the mean and an error on  
1186 the width of this probability distribution is calculated using the approach highlighted  
1187 in subsection 3.3.2. Consequently, the best fit distribution in the fit parameter is not  
1188 necessarily that which would be attained by reweighting the Monte Carlo prediction  
1189 to the most probable parameter values.

1190 A similar study can be performed to illustrate the freedom of the model parameter  
1191 space prior to the fit. This can be done by throwing parameter values from the prior  
1192 uncertainty of each parameter. This becomes troublesome for parameters with no  
1193 prior uncertainty as the range is technically infinite. Where applicable solutions to  
1194 remove these have been addressed.

<sub>1195</sub> **Chapter 4**

<sub>1196</sub> **Oscillation Probability Calculation**

<sub>1197</sub> Oscillation calculation

<sub>1198</sub> **4.1 Super-Kamiokande Methodology**

<sub>1199</sub> SK Method Section

<sub>1200</sub>

<sub>1201</sub> **Bibliography**

- <sub>1202</sub> [1] J. Chadwick, Verhandl. Dtsc. Phys. Ges. **16**, 383 (1914).
- <sub>1203</sub> [2] C. D. Ellis and W. A. Wooster, Proc. R. Soc. Lond. A Math. Phys. Sci. **117**, 109  
<sub>1204</sub> (1927).
- <sub>1205</sub> [3] W. Pauli, Phys. Today **31N9**, 27 (1978).
- <sub>1206</sub> [4] E. Fermi, Z. Phys. **88**, 161 (1934).
- <sub>1207</sub> [5] F. Reines and C. L. Cowan, Phys. Rev. **92**, 830 (1953).
- <sub>1208</sub> [6] C. L. Cowan, F. Reines, F. B. Harrison, H. W. Kruse, and A. D. McGuire, Science  
<sub>1209</sub> **124**, 103 (1956), <http://science.sciencemag.org/content/124/3212/103.full.pdf>.
- <sub>1210</sub> [7] G. Danby *et al.*, Phys. Rev. Lett. **9**, 36 (1962).
- <sub>1211</sub> [8] K. Kodama *et al.*, Physics Letters B **504**, 218 (2001).
- <sub>1212</sub> [9] LSND, A. Aguilar-Arevalo *et al.*, Phys. Rev. **D64**, 112007 (2001), hep-ex/0104049.
- <sub>1213</sub> [10] MiniBooNE Collaboration, A. A. Aguilar-Arevalo *et al.*, Phys. Rev. Lett. **110**,  
<sub>1214</sub> 161801 (2013).
- <sub>1215</sub> [11] and P. A. R. Ade *et al.*, Astronomy and Astrophysics **594**, A13 (2016).
- <sub>1216</sub> [12] B. Pontecorvo, Sov. Phys. JETP **26**, 984 (1968), [Zh. Eksp. Teor. Fiz. 53, 1717 (1967)].
- <sub>1217</sub> [13] B. Pontecorvo, Sov. Phys. JETP **7**, 172 (1958), [Zh. Eksp. Teor. Fiz. 34, 247 (1957)].
- <sub>1218</sub> [14] M. Kobayashi and T. Maskawa, Progress of Theoretical Physics **49**, 652 (1973).
- <sub>1219</sub> [15] N. Cabibbo, Phys. Rev. Lett. **10**, 531 (1963).
- <sub>1220</sub> [16] A. Y. Smirnov, (2003).
- <sub>1221</sub> [17] S. Mikheyev and A. Smirnov, Soviet Journal of Nuclear Physics **42**, 913 (1985).
- <sub>1222</sub> [18] L. Wolfenstein, Phys. Rev. D **17**, 2369 (1978).
- <sub>1223</sub> [19] A. M. Dziewonski and D. L. Anderson, Phys. Earth Planet. Inter. **25**, 297 (1981).
- <sub>1224</sub> [20] R. Wendell, *Three Flavor Oscillation Analysis of Atmospheric Neutrinos in Super-Kamiokande*, PhD thesis, University of North Carolina, 2008.  
<sub>1225</sub>

- [21] The Super-Kamiokande Collaboration, Y. Ashie *et al.*, Phys. Rev. Lett. **93**, 101801 (2004).
- [22] SNO Collaboration, Q. R. Ahmad *et al.*, Phys. Rev. Lett. **89**, 011301 (2002).
- [23] 2015 Nobel prize in Physics as listed by Nobelprize.org, [https://www.nobelprize.org/nobel\\_prizes/physics/laureates/2015/](https://www.nobelprize.org/nobel_prizes/physics/laureates/2015/), Accessed: 18-04-2018.
- [24] J. A. Formaggio and G. P. Zeller, Rev. Mod. Phys. **84**, 1307 (2012), 1305.7513.
- [25] A. Bellerive, Int. J. Mod. Phys. A **19**, 1167 (2004).
- [26] R. Davis, D. S. Harmer, and K. C. Hoffman, Phys. Rev. Lett. **20**, 1205 (1968).
- [27] N. Vinyoles *et al.*, Astrophys. J. **835**, 202 (2017).
- [28] V. Gribov and B. Pontecorvo, Phys. Lett. B **28**, 493 (1969).
- [29] K. S. Hirata *et al.*, Phys. Rev. Lett. **63**, 16 (1989).
- [30] W. Hampel *et al.*, Phys. Lett. B **447**, 127 (1999).
- [31] SAGE Collaboration, J. N. Abdurashitov *et al.*, Phys. Rev. C **60**, 055801 (1999).
- [32] Q. R. Ahmad *et al.*, Phys. Rev. Lett. **89** (2002).
- [33] Borexino Collaboration, Nature **562**, 505 (2018).
- [34] B. Aharmim *et al.*, Astrophys. J. **653**, 1545 (2006).
- [35] M. Agostini *et al.*, (2020).
- [36] S. Andringa *et al.*, Adv. High Energy Phys. **2016**, 1 (2016).
- [37] J. F. Beacom *et al.*, Chin. phys. C **41**, 023002 (2017).
- [38] F. An *et al.*, J. Phys. G Nucl. Part. Phys. **43**, 030401 (2016).
- [39] J. Aalbers *et al.*, (2020), 2006.03114.
- [40] T. K. Gaisser and M. Honda, (2002).
- [41] G. D. Barr, T. K. Gaisser, P. Lipari, S. Robbins, and T. Stanev, Physical Review D **70** (2004).
- [42] M. Honda, T. Kajita, K. Kasahara, S. Midorikawa, and T. Sanuki, Physical Review

- 1252 D **75** (2007).
- 1253 [43] M. Honda, T. Kajita, K. Kasahara, and S. Midorikawa, Phys. Rev. D **70**, 043008  
1254 (2004).
- 1255 [44] A. Fasso, A. Ferrari, P. R. Sala, and J. Ranft, (2001).
- 1256 [45] Y. Ashie *et al.*, Physical Review D **71** (2005).
- 1257 [46] F. Reines *et al.*, Phys. Rev. Lett. **15**, 429 (1965).
- 1258 [47] D. Casper *et al.*, Phys. Rev. Lett. **66**, 2561 (1991).
- 1259 [48] K. S. Hirata *et al.*, Phys. Lett. B **280**, 146 (1992).
- 1260 [49] Z. Li *et al.*, Physical Review D **98** (2018).
- 1261 [50] Kamiokande Collaboration *et al.*, (2017).
- 1262 [51] T2K Collaboration, Nature **580**, 339 (2020).
- 1263 [52] M. A. Acero *et al.*, Phys. Rev. Lett. **123**, 151803 (2019).
- 1264 [53] M. G. Aartsen *et al.*, Phys. Rev. Lett. **120** (2018).
- 1265 [54] P. Adamson *et al.*, Phys. Rev. Lett. **112** (2014).
- 1266 [55] M. S. Athar *et al.*, Progress in Particle and Nuclear Physics **124**, 103947 (2022).
- 1267 [56] G. Danby *et al.*, Phys. Rev. Lett. **9**, 36 (1962).
- 1268 [57] K. Abe *et al.*, Physical Review D **87** (2013).
- 1269 [58] MINOS Collaboration, D. G. Michael *et al.*, Phys. Rev. Lett. **97**, 191801 (2006).
- 1270 [59] G. Danby *et al.*, Phys. Rev. Lett. **9**, 36 (1962).
- 1271 [60] NOvA Collaboration, M. A. Acero *et al.*, Phys. Rev. Lett. **123**, 151803 (2019).
- 1272 [61] B. Abi, R. Acciarri, M. A. Acero, and G. e. a. Adamov, Eur. Phys. J. C Part. Fields  
1273 **80** (2020).
- 1274 [62] Hyper-Kamiokande Proto-Collaboration *et al.*, Prog. Theor. Exp. Phys. **2015**,  
1275 53C02 (2015).
- 1276 [63] C. Blanco, D. Hooper, and P. Machado, Physical Review D **101** (2020).
- 1277 [64] MicroBooNE Collaboration *et al.*, Search for an Excess of Electron Neutrino

- 1278        Interactions in MicroBooNE Using Multiple Final State Topologies, 2021.
- 1279 [65] KARMEN Collaboration, B. Armbruster *et al.*, Phys. Rev. D **65**, 112001 (2002).
- 1280 [66] S.-B. Kim, T. Lasserre, and Y. Wang, Adv. High Energy Phys. **2013**, 1 (2013).
- 1281 [67] M. Sajjad Athar *et al.*, Prog. Part. Nucl. Phys. **124**, 103947 (2022), 2111.07586.
- 1282 [68] K. Abe *et al.*, Nucl. Instrum. Methods Phys. Res. A **1027**, 166248 (2022).
- 1283 [69] F. P. An *et al.*, Phys. Rev. Lett. **108**, 171803 (2012).
- 1284 [70] RENO Collaboration, J. K. Ahn *et al.*, Phys. Rev. Lett. **108**, 191802 (2012).
- 1285 [71] Double Chooz Collaboration, Y. Abe *et al.*, Phys. Rev. Lett. **108**, 131801 (2012).
- 1286 [72] J. Collaboration *et al.*, TAO Conceptual Design Report: A Precision Measurement  
1287        of the Reactor Antineutrino Spectrum with Sub-percent Energy Resolution, 2020,  
1288        2005.08745.
- 1289 [73] for the RENO Collaboration, New results from RENO and the 5 MeV excess,  
1290        AIP Publishing LLC, 2015.
- 1291 [74] Y. Abe *et al.*, Journal of High Energy Physics **2014** (2014).
- 1292 [75] Daya Bay Collaboration, D. Adey *et al.*, Phys. Rev. Lett. **123**, 111801 (2019).
- 1293 [76] M. P. Decowski, Nucl. Phys. B. **908**, 52 (2016).
- 1294 [77] The KamLAND Collaboration, A. Gando *et al.*, Phys. Rev. D **83**, 052002 (2011).
- 1295 [78] Y. Fukuda *et al.*, Phys. Rev. Lett. **81**, 1562 (1998).
- 1296 [79] K. Abe *et al.*, Nuclear Instruments and Methods in Physics Research Section  
1297        A: Accelerators, Spectrometers, Detectors and Associated Equipment **737**, 253  
1298        (2014).
- 1299 [80] S. Fukuda *et al.*, Nucl. Instrum. Methods Phys. Res. A **501**, 418 (2003).
- 1300 [81] Y. Itow *et al.*, (2001).
- 1301 [82] M. Jiang *et al.*, Prog. Theor. Exp. Phys. **2019** (2019).
- 1302 [83] S. Fukuda *et al.*, Nuclear Instruments and Methods in Physics Research Section  
1303        A: Accelerators, Spectrometers, Detectors and Associated Equipment **501**, 418  
1304        (2003), <http://www.sciencedirect.com/science/article/pii/S016890020300425X>.

- 1305 [84] Y. Nakano *et al.*, Nucl. Instrum. Methods Phys. Res. A **977**, 164297 (2020).
- 1306 [85] Hamamatsu, Hamamatsu Photonics Photomultiplier Tubes Handbook.
- 1307 [86] K. Abe *et al.*, Nucl. Instrum. Methods Phys. Res. A **1027**, 166248 (2022).
- 1308 [87] J. F. Beacom and M. R. Vagins, Phys. Rev. Lett. **93**, 171101 (2004).
- 1309 [88] L. Marti *et al.*, Nucl. Instrum. Methods Phys. Res. A **959**, 163549 (2020).
- 1310 [89] L. Marti *et al.*, (2019).
- 1311 [90] G. Carminati, Phys. Procedia **61**, 666 (2015).
- 1312 [91] T. Tanimori *et al.*, IEEE Transactions on Nuclear Science **36**, 497 (1989).
- 1313 [92] Super-Kamiokande Collaboration, J. Hosaka *et al.*, Phys. Rev. D **73**, 112001  
1314 (2006).
- 1315 [93] H. Nishino *et al.*, Nucl. Instrum. Methods Phys. Res. A **610**, 710 (2009).
- 1316 [94] S. Yamada *et al.*, IEEE Transactions on Nuclear Science **57**, 428 (2010).
- 1317 [95] S. Yamada, Y. Hayato, Y. Obayashi, and M. Shiozawa, New online system  
1318 without hardware trigger for the Super-Kamiokande experiment, in *2007 IEEE  
1319 Nuclear Science Symposium Conference Record*, IEEE, 2007.
- 1320 [96] P. A. Čerenkov, Phys. Rev. **52**, 378 (1937).
- 1321 [97] I. Frank and I. Tamm, Coherent visible radiation of fast electrons passing  
1322 through matter, in *Selected Papers*, pp. 29–35, Springer Berlin Heidelberg, Berlin,  
1323 Heidelberg, 1991.
- 1324 [98] The T2K Collaboration, KEK Proposal (2001),  
1325 <http://neutrino.kek.jp/jhfnu/loi/loi.v2.030528.pdf>.
- 1326 [99] Y. Itow *et al.*, (2001), hep-ex/0106019.
- 1327 [100] The K2K Collaboration and S. H. Ahn, (2001), hep-ex/0103001.
- 1328 [101] The T2K Collaboration, KEK Proposal (2006), [http://j-parc.jp/researcher/Hadron/en/pac\\_0606/pdf/p11-Nishikawa.pdf](http://j-parc.jp/researcher/Hadron/en/pac_0606/pdf/p11-Nishikawa.pdf).
- 1330 [102] T2K Collaboration, K. Abe *et al.*, Phys. Rev. Lett. **112**, 061802 (2014),  
1331 <https://link.aps.org/doi/10.1103/PhysRevLett.112.061802>.

- 1332 [103] NINJA Collaboration, T. Fukuda *et al.*, Proposal for precise measurement of  
1333 neutrino-water cross-section in NINJA physics run, Proposal for J-PARC and  
1334 KEK, 2017.
- 1335 [104] T. Ovsianikova *et al.*, Physics of Particles and Nuclei **48**, 1014 (2017),  
1336 <https://doi.org/10.1134/S1063779617060478>.
- 1337 [105] M. Antonova *et al.*, Journal of Instrumentation **12**, C07028 (2017),  
1338 <http://stacks.iop.org/1748-0221/12/i=07/a=C07028>.
- 1339 [106] The T2K Collaboration, K. Abe *et al.*, Phys. Rev. D **102**, 012007 (2020).
- 1340 [107] K. Abe *et al.*, Progress of Theoretical and Experimental Physics **2021** (2021).
- 1341 [108] The T2K Collaboration, K. Abe *et al.*, Nuclear Instruments  
1342 and Methods in Physics Research Section A: Accelerators, Spec-  
1343 trometers, Detectors and Associated Equipment **659**, 106 (2011),  
1344 <http://www.sciencedirect.com/science/article/pii/S0168900211011910>.
- 1345 [109] K. Matsuoka *et al.*, Nuclear Instruments and Methods in Physics Research Section  
1346 A: Accelerators, Spectrometers, Detectors and Associated Equipment **624**, 591  
1347 (2010), <http://www.sciencedirect.com/science/article/pii/S016890021002098X>.
- 1348 [110] K. Abe *et al.*, Phys. Rev. D. **103** (2021).
- 1349 [111] T. Vladisavljevic, *Predicting the T2K neutrino flux and measuring oscillation parame-*  
1350 *ters* Springer theses, 1 ed. (Springer Nature, Cham, Switzerland, 2020).
- 1351 [112] D. Beavis, A. Carroll, and I. Chiang, (1995).
- 1352 [113] P.-A. Amaudruz *et al.*, Nuclear Instruments and Methods in Physics Research  
1353 Section A: Accelerators, Spectrometers, Detectors and Associated Equipment  
1354 **696**, 1 (2012).
- 1355 [114] N. Abgrall *et al.*, Nuclear Instruments and Methods in Physics Research Section  
1356 A: Accelerators, Spectrometers, Detectors and Associated Equipment **637**, 25  
1357 (2011).
- 1358 [115] S. Assylbekov *et al.*, Nuclear Instruments and Methods in Physics Research  
1359 Section A: Accelerators, Spectrometers, Detectors and Associated Equipment  
1360 **686**, 48 (2012).
- 1361 [116] D. Allan *et al.*, Journal of Instrumentation **8**, P10019 (2013).

- 1362 [117] F. Vannucci, Advances in High Energy Physics **2014**, 1 (2014).
- 1363 [118] UA1 magnet sets off for a second new life, 2022.
- 1364 [119] S. Aoki *et al.*, Nuclear Instruments and Methods in Physics Research Section  
1365 A: Accelerators, Spectrometers, Detectors and Associated Equipment **698**, 135  
1366 (2013).
- 1367 [120] M. Yokoyama *et al.*, Nuclear Instruments and Methods in Physics Research  
1368 Section A: Accelerators, Spectrometers, Detectors and Associated Equipment  
1369 **622**, 567 (2010).
- 1370 [121] K. Suzuki *et al.*, Progress of Theoretical and Experimental Physics **2015**, 53C01  
1371 (2015).
- 1372 [122] S. Brooks, A. Gelman, G. L. Jones, and X.-L. Meng, *Handbook of Markov Chain  
Monte Carlo* (CRC Press, 2011).
- 1374 [123] W. R. Gilks, S. Richardson, and D. J. Spiegelhalter, *Markov Chain Monte Carlo in  
Practice* (Chapman & Hall/CRC Interdisciplinary Statistics, 1995).
- 1376 [124] C. Wret, *Minimising systematic uncertainties in the T2K experiment using near-  
1377 detector and external data*, PhD thesis, Imperial College London, 2018.
- 1378 [125] K. E. Duffy, *Measurement of the Neutrino Oscillation Parameters  $\sin^2 \theta_{23}$ ,  $\Delta m_{32}^2$ ,  
1379  $\sin^2 \theta_{13}$ , and  $\delta_{CP}$  in Neutrino and Antineutrino Oscillation at T2K*, PhD thesis, Oriel  
1380 College, University of Oxford, 2016.
- 1381 [126] T. Bayes, Rev. Phil. Trans. Roy. Soc. Lond. **53**, 370 (1764).
- 1382 [127] N. Metropolis, A. W. Rosenbluth, M. N. Rosenbluth, A. H. Teller, and E. Teller,  
1383 Journal of Chemical Physics **21** (1970).
- 1384 [128] W. K. Hastings, Biometrika **57** (1970).
- 1385 [129] J. Dunkley, M. Bucher, P. G. Ferreira, K. Moodley, and C. Skordis, Mon. Not. R.  
1386 Astron. Soc. **356**, 925 (2005).
- 1387 [130] Particle Data Group *et al.*, Prog. Theor. Exp. Phys. **2020** (2020).
- 1388 [131] H. Jeffreys, *The Theory of Probability* Oxford Classic Texts in the Physical Sciences  
1389 (, 1939).
- 1390 [132] R. E. Kass and A. E. Raftery, J. Am. Stat. Assoc. **90**, 773 (1995).

# <sup>1391</sup> List of Figures

<sup>1392</sup>	1.1	The cross-section of neutrinos from various natural and man-made sources as a function of neutrino energy. Taken from [24] . . . . .	8
<sup>1393</sup>			
<sup>1394</sup>	1.2	The solar neutrino flux as a function of neutrino energy for various fusion reactions and decay chains as predicted by the Standard Solar Model. Taken from [25]. . . . .	9
<sup>1395</sup>			
<sup>1396</sup>			
<sup>1397</sup>	1.3	Left panel: The atmospheric neutrino flux for different neutrino flavours as a function of neutrino energy as predicted by the 2007 Honda model (“This work”) [42], the 2004 Honda model (“HKKM04”) [43], the Bartol model [41] and the FLUKA model [44]. Right panel: The ratio of the muon to electron neutrino flux as predicted by all the quoted models. Both figures taken from [42]. . . . .	11
<sup>1398</sup>			
<sup>1399</sup>			
<sup>1400</sup>			
<sup>1401</sup>			
<sup>1402</sup>			
<sup>1403</sup>	1.4	A diagram illustrating the definition of zenith angle as used in the Super Kamiokande experiment [45]. . . . .	12
<sup>1404</sup>			
<sup>1405</sup>	1.5	Predictions of the summed neutrino and antineutrino flux for electron and muon neutrinos from the Bartol [41], Honda [42] and FLUKA [44] models as a function of zenith angle with respect to the detector. Left panel: $0.3 < E_\nu < 0.5$ . Middle panel: $0.9 < E_\nu < 1.5$ . Right panel: $3.0 < E_\nu < 5.0$ . Figures taken from [45]. . . . .	13
<sup>1406</sup>			
<sup>1407</sup>			
<sup>1408</sup>			
<sup>1409</sup>			
<sup>1410</sup>	1.6	Constraints on the atmospheric oscillation parameters, $\sin^2(\theta_{23})$ and $\Delta m_{23}^2$ , from atmospheric and long baseline experiments: SK [50], T2K [51], NO $\nu$ A [52], IceCube [53] and MINOS [54]. Figure taken from [55].	14
<sup>1411</sup>			
<sup>1412</sup>			
<sup>1413</sup>	1.7	Reactor electron antineutrino fluxes for $^{235}\text{U}$ (Black), $^{238}\text{U}$ (Green), $^{239}\text{Pu}$ (Purple), and $^{241}\text{Pu}$ (Orange) isotopes. The inverse $\beta$ -decay cross-section (Blue) and corresponding measurable neutrino spectrum (Red) are also given. Top panel: Schematic of Inverse $\beta$ -decay interaction including the eventual capture of the emitted neutron. This capture emits a $\gamma$ -ray which provides a second signal of the event. Taken from [67]. . . . .	16
<sup>1414</sup>			
<sup>1415</sup>			
<sup>1416</sup>			
<sup>1417</sup>			
<sup>1418</sup>			
<sup>1419</sup>	2.1	A schematic diagram of the Super-Kamiokande Detector. Taken from [81].	19

1420	2.2	The location of “standard PMTs” (red) inside the SK detector. Taken from [79]. . . . .	21
1421			
1422	2.3	Schematic view of the data flow through the data acquisition and online system. Taken from [94]. . . . .	24
1423			
1424	2.4	The cross-section view of the Tokai to Kamioka experiment illustrating the beam generation facility at J-PARC, the near detector situated at a baseline of 280m and the Super Kamiokande far detector situated 295km from the beam target. . . . .	27
1425			
1426			
1427			
1428	2.5	The near detector suite for the T2K experiment showing the ND280 and INGRID detectors. The distance between the detectors and the beam target is 280m. . . . .	28
1429			
1430			
1431	2.6	Top panel: Bird’s eye view of the most relevant part of primary and secondary beamline used within the T2K experiment. The primary beamline is the main-ring proton synchrotron, kicker magnet, and graphite target. The secondary beamline consists of the three focusing horns, decay volume, and beam dump. Figure taken from [108]. Bottom panel: The side-view of the secondary beamline including the focusing horns, beam dump and neutrino detectors. Figure taken from [109]. . . . .	29
1432			
1433			
1434			
1435			
1436			
1437			
1438	2.7	The Monte Carlo prediction of the energy spectrum for each flavour of neutrino ( $\nu_e$ , $\bar{\nu}_e$ , $\nu_\mu$ and $\bar{\nu}_\mu$ ) in the neutrino dominated beam FHC mode (Left) and antineutrino dominated beam RHC mode (Right) expected at SK. Taken from [110]. . . . .	31
1439			
1440			
1441			
1442	2.8	Top panel: T2K muon neutrino disappearance probability as a function of neutrino energy. Middle panel: T2K electron neutrino appearance probability as a function of neutrino energy. Bottom panel: The neutrino flux distribution for three different off-axis angles (Arbitrary units) as a function of neutrino energy. . . . .	32
1443			
1444			
1445			
1446			
1447	2.9	The components of the ND280 detector. The neutrino beam travels from left to right. Taken from [108]. . . . .	33
1448			
1449	2.10	Comparison of data to Monte Carlo prediction of integrated deposited energy as a function of track length for particles that stopped in FGD1. Taken from [113]. . . . .	34
1450			
1451			

1452	2.11 Schematic design of a Time Projection Chamber detector. Taken from [114].	35
1453	2.12 The distribution of energy loss as a function of reconstructed momentum for charged particles passing through the TPC, comparing data to Monte Carlo prediction. Taken from [114].	36
1455		
1456	2.13 A schematic of the P0D side-view. Taken from [115].	37
1457	2.14 Left panel: The Interactive Neutrino GRID on-axis Detector. 14 modules are arranged in a cross-shape configuration, with the center modules being directly aligned with the on-axis beam. Right panel: The layout of a single module of the INGRID detector. Both figures are recreated from [108].	39
1459		
1460		
1461		
1462	3.1 Example of using Monte Carlo techniques to find the area under the blue line. The gradient and intercept of the line are 0.4 and 1.0 respectively. The area found to be under the curve using one thousand samples is 29.9 units.	43
1463		
1464		
1465		
1466	3.2 The area under a line of gradient 0.4 and intercept 1.0 for the range $0 \leq x \leq 10$ as calculated using Monte Carlo techniques as a function of the number of samples used in each repetition. The analytical solution to the area is 30 units as given by the red line.	44
1467		
1468		
1469		
1470	3.3 Three MCMC chains, each with a stationary distribution equal to a Gaussian centered at 0 and width 1 (As indicated by the black dotted lines). All of the chains use a Gaussian proposal function but have different widths (or 'step size $\sigma$ '). The top panel has $\sigma = 0.1$ , middle panel has $\sigma = 0.5$ and the bottom panel has $\sigma = 5.0$ .	48
1471		
1472		
1473		
1474		
1475	3.4 The log-likelihood from the fit detailed in <a href="#">DB: Link to AsimovA Sensitivity Section</a> as a function of the number of steps accumulated in each fit. Many independent MCMC chains were run in parallel and overlaid on this plot. The red line indicates the $1 \times 10^5$ step burn-in period after which the log-likelihood becomes stable.	49
1476		
1477		
1478		
1479		



# <sup>1486</sup> List of Tables

<sup>1487</sup> 1.1	Description of the four layers of the Earth invoked within the PREM model [19]. . . . .	<sup>1488</sup> 7
<sup>1489</sup> 2.1	The various SK periods and respective live-time. The SK-VI live-time is calculated until 1 <sup>st</sup> April 2022. SK-VII started during the writing of this thesis. . . . .	<sup>1490</sup> 18
<sup>1492</sup> 2.2	The trigger thresholds and extended time windows saved around an event which were utilised throughout the SK-IV period. The exact thresholds can change and the values listed here represent the thresholds at the start and end of the SK-IV period. . . . .	<sup>1493</sup> 25
<sup>1496</sup> 2.3	The threshold momentum and energy for a particle to generate Cherenkov light in ultrapure water, as calculated in Equation 2.2 in ultrapure water which has refractive index $n = 1.33$ . . . . .	<sup>1497</sup> 26
<sup>1499</sup> 3.1	Jeffreys scale for strength of preference for two models $A$ and $B$ as a function of the calculated Bayes factor ( $B_{AB} = B(A/B)$ ) between the two models [131]. The original scale is given in terms of $\log_{10}(B(A/B))$ but converted to linear scale for easy comparison throughout this thesis.	<sup>1500</sup> 53
<sup>1501</sup>		<sup>1502</sup>